

# Development of Figure-of-Nine Laser Cavity for Mode-Locked Fiber Lasers: A Review

Kuen Yao Lau, Zhichao Luo, Jinwen Lin, Beibei Xu, Xiaofeng Liu,\* and Jianrong Qiu\*

Artificial saturable absorbers (SA) are nonlinear optical devices widely employed in mode-locked lasers. Among the artificial SAs are nonlinear polarization evolution (NPE) and nonlinear amplifying loop mirrors that can work in either figure-of-eight (Fo8) or figure-of-nine (Fo9) laser cavities. The NPE technique is highly sensitive to environmental perturbations. Both Fo8 and Fo9 laser cavities exhibit a higher environmental stability than the NPE technique. Here the recent advances of the Fo9 laser cavity, with a focus on the pulse formation mechanisms and the role of different cavity parameters that can enable ultrafast mode-locking analyses are discussed. Besides, the recent development of using the Fo9 laser cavity to generate high-energy rectangular laser pulses through either dissipative soliton resonance or noise-like pulse regimes is also reviewed. In conclusion, the current issues and challenges of pulse formation through the Fo9 laser cavity are highlighted and recommendations for future research directions are proposed. This review is expected to provide a deeper insight into the Fo9 laser cavity as the next generation of artificial SA with interesting cavity structures, laser features, and output performances.

## 1. Introduction

Mode-locked lasers with ultrafast pulse output are attractive for a plethora of applications in fields such as micromachining, metrology, optical frequency combs, and nonlinear optics.<sup>[1–3]</sup> Among various types of mode-locked lasers, fiber lasers exhibit compact footprints, robustness, stability, and excellent beam quality.<sup>[4,5]</sup> More than thousands of longitudinal modes must be locked together to support a reliable and self-starting passive mode-locked fiber laser (MLFL) through either material-based or artificial saturable absorbers (SAs).<sup>[6]</sup> Intrinsic SAs, such as a semiconductor saturable absorber mirror (SESAM), and low-dimensional materials, such as carbon nanotube (CNT) and graphene, are suitable SA candidates.<sup>[7–9]</sup> Intrinsic or material-based SAs generate mode-locking pulse output through saturable absorption, while the transmission

reaches a maximum or the optical loss greatly reduces at high optical intensity. The intrinsic SA, e.g., the SESAM was demonstrated for the first time by Keller et al.<sup>[10]</sup> to initiate mode-locking in 1992. An anti-reflection-coated SESAM has a shortcoming of limited bandwidth from the Bragg reflector, which can be replaced by a metal reflector to obtain larger bandwidth.<sup>[11]</sup> In addition, the SESAM comes with some drawbacks such as lower damage threshold and shorter lifetime under higher saturation fluence and faster carrier relaxation time.<sup>[12]</sup> For instance, the SESAM encounters critical optical degradation with faster decay time under higher saturation fluence. Moreover, the lifetime of a SESAM was decreased from 4000 to 1000 h due to an increase in carrier relaxation (15–1 ps). Apart from SESAM, material-based SA thin films have been widely used in MLFLs. The mode-locked pulse formation through material-based SA thin films such as CNT and graphene, which were first demonstrated by Set et al.<sup>[13]</sup> in 2003 and Bao et al.<sup>[14]</sup> in 2009, respectively. The historical development of CNT and graphene SAs for mode-locked fiber lasers was described in our previous review.<sup>[9]</sup> Liu et al. presented the CNT-SA with different modulation depth and non-saturable loss,<sup>[15]</sup> which was typically characterized through an I-scan method.<sup>[16]</sup> In the pulse formation of mode-locking, a CNT-SA with a higher modulation depth and a lower non-saturable loss can reduce the buildup time prior to the formation of mode-locking, due to the suppression of an unstable Q-switched lasing state.<sup>[17]</sup> Nevertheless, the incorporation of a material-based SA

K. Y. Lau  
School of Optoelectronic Science and Engineering and Collaborative  
Innovation Center of Suzhou Nano Science and Technology  
Soochow University  
Suzhou 215006, China

K. Y. Lau  
Key Lab of Advanced Optical Manufacturing Technologies of Jiangsu  
Province and Key Lab of Modern Optical Technologies of Education  
Ministry of China  
Soochow University  
Suzhou 215006, China

Z. Luo  
Guangdong Provincial Key Laboratory of Nanophotonic Functional  
Materials and Devices  
South China Normal University  
Guangzhou, Guangdong 510006, China

J. Lin, B. Xu, J. Qiu  
College of Optical Science and Engineering and State Key Lab of Modern  
Optical Instrumentation  
Zhejiang University  
Hangzhou 310027, China  
E-mail: qjr@zju.edu.cn

X. Liu  
School of Materials Science and Engineering  
Zhejiang University  
Hangzhou 310027, China  
E-mail: xfliu@zju.edu.cn

DOI: 10.1002/lpor.202301239

into a fiber laser cavity requires the formulation of a method to achieve proper interaction with light. The reproducibility of the SA fabrication may pose a challenge because of the need for reproducible thin films to be incorporated into a laser cavity structure that demands advanced techniques.<sup>[18]</sup> In addition, material-based SAs exhibit low damage thresholds and they tend to degrade over time.<sup>[19,20]</sup>

Apart from material-based SAs, a Mamyshev laser is an excellent SA alternative which is the most adjustable, configurable, and controllable one, even on the fly. The Mamyshev laser works well with the polarization-maintaining fibers, making it environmentally robust. The term “Mamyshev” laser was given name because this laser configuration was first presented by Mamyshev in 1998,<sup>[21]</sup> which can support any of the pulse operation schemes, whether it is soliton, stretched-pulse, similariton, or dissipative soliton lasers. Wise et al. conducted some Mamyshev laser works with their first article focused on generating megawatt peak power.<sup>[22]</sup> The Mamyshev laser is useful for generating high peak power, however, the main shortcoming of the Mamyshev laser is that it is not self-starting.

Apart from material-based SA and Mamyshev laser, artificial SAs based on nonlinear effects inside the laser cavity give rise to an additive pulse mode-locking (APM) schemes, which have been used in fiber lasers since the early 1990s.<sup>[23]</sup> In contrast to material-based SAs, the APM offers advantages such as ultrafast recovery time, lower intrinsic noise, higher damage threshold, cost-effectiveness, and negligible performance degradation over time.<sup>[19,24]</sup> The APM works on a coherent interferometric addition of pulses that induces intensity-dependent loss with different phases, which depends on the pulse intensity. The phase difference can be provided by birefringence, nonlinear phase shift, and phase bias. The phase difference due to birefringence is contributed by the propagation of laser pulses in different polarization states of a birefringent medium. The phase difference due to nonlinear phase shift or phase bias is induced by self-phase modulation experienced by the laser pulses with different intensities which propagates in a nonlinear medium via optical Kerr effect.<sup>[25]</sup> The phase modulation in a fiber laser cavity accumulates intensity-dependent nonlinear phase shifts or a phase bias which reduces the intracavity nonlinear intensity losses at high intensities, thus forming an artificial SA.<sup>[26]</sup>

Nonlinear polarization evolution (NPE) is an example of artificial SA. The original work on the NPE was demonstrated by Hofer et al. in 1991, who presented a highly nonlinear laser cavity by the NPE based on self-phase and cross-phase modulations.<sup>[27]</sup> Subsequently, non-reciprocal pulse shaping was obtained in a slightly linear birefringent fiber inserted into a single-polarization Fabry–Perot cavity. The NPE is highly sensitive to environmental perturbations. Conventional single-mode fibers are typically used in fiber laser systems, where the non-polarization maintaining characteristics contribute to the high sensitivity of the propagation light beam toward environmental perturbations.<sup>[28]</sup> For instance, optical frequency combs working on the NPE regime are sensitive to environmental perturbations, such as temperature, pressure, and vibration, which cause a change in polarization, a decrease in frequency comb performance, or even a complete loss of mode-locking operation.<sup>[29]</sup> This means that mode-locking based on NPE may be working inside laboratories but it could be undeployable outside labora-

tories. A good solution to combat environmental perturbations is the incorporation of a polarization-maintaining (PM) fiber.<sup>[30]</sup> The linear polarization state of a propagating light beam can be maintained inside the PM fiber, thus realizing an environmentally stable MLFL. Substantial efforts were made to realize NPE with an all-PM structure, which requires splicing the PM fiber at a precise angle or using other optimization methods, which increases complexity and additional losses to the laser cavity.<sup>[31,32]</sup>

Apart from the NPE, nonlinear optical loop mirrors (NOLM) and nonlinear amplifying loop mirror (NALM) are two other types of artificial SAs, which were first demonstrated by Doran et al.<sup>[33]</sup> in 1988 and Fermann et al.<sup>[34]</sup> in 1990, respectively. Doran and coworkers introduced a nonlinear device for ultrafast processing based on the nonlinear propagation in a waveguide loop by connecting the output ports of a coupler with unequal coupling ratios to form the NOLM, whereas Fermann and coworkers proposed the NALM using a long optical fiber loop mirror with an integral short asymmetrically located optical amplifier. In contrast to the NPE technique, both NOLM and NALM do not rely on polarization and can be easily integrated into an all-PM fiber laser design, thus exhibiting fewer instabilities that may result in weak self-starting or multi-pulsing.<sup>[35–38]</sup> The transmission or reflection of both NOLM and NALM are based on differences in the nonlinear phase shift between counter-propagating beams. Since the nonlinear phase shift is intensity-dependent, these devices can operate as SAs and thus support mode-locking if the NOLM or NALM is incorporated such that the total laser cavity round-trip loss decreases as soon as the nonlinear phase shift deviates from zero. The splitting ratio between the counter-propagating beams determines the roundtrip transmission of the mirror loop and the interference conditions. The difference in roundtrip transmission results in nonlinear phase shift, which is an effect of the asymmetry of the coupling ratio for the NOLM or a result of the asymmetry of active fiber position for the NALM. A well-known NOLM or NALM structure is the Figure-of-Eight (Fo8) laser cavity. A drawback of the Fo8 fiber laser is the difficulty of self-start mode-locking due to the limited peak power sensitivity and weak intensity dependence caused by the phase difference between the counter-propagating beams. To improve self-start mode-locking ability, the most practical method is to employ the combination of a Fo8 laser cavity with a physical saturable absorber.<sup>[39]</sup> The physical SA was placed between the NOLM and the gain fiber to improve pulse self-starting ability. Without this physical SA, the pulse operation was achieved with reduced stability, thus an external perturbation is required to assist initial pulse formation. Besides, the mode-locking in the Fo8 laser cavity can also be self-started by placing an electro-optic modulator<sup>[40]</sup> or acousto-optic modulator<sup>[41]</sup> at an asymmetric position in a NOLM or NALM. The modulators induce phase difference ( $\Delta\varphi$ ) between counter-propagating beams according to:

$$\Delta\varphi = \frac{2\pi n (L_1 - L_2) \Delta f}{c} \quad (1)$$

where  $n$  is the refractive index of the fiber,  $L_1$  and  $L_2$  are the fiber length from the coupler to the modulator in the clockwise (CW) and counter-clockwise (CCW) direction, and  $\Delta f$  is the frequency shift. The modulation of  $\Delta f$  contributes to an arbitrary phase shift. Without the additional cavity modulation introduced by the

modulator, a large asymmetric coupling ratio can be incorporated to initiate mode-locking operation at the expense of additional loss which is not suitable for operation with low intrinsic noise.

Therefore, more robust mode-locking techniques with better mode-locking initiation regimes are desirable. Carruthers et al.<sup>[42]</sup> demonstrated the first sigma laser which has the shape of a Figure-of-Nine (Fo9) cavity in 1994. In this sigma laser cavity, active mode-locking was achieved in the PM ring cavity. A birefringent waveplate was placed between a polarizer (polarizing beam-splitter) and a Faraday rotator (FR), which was then coupled into a fiber amplifier (erbium-doped fiber amplifier). The birefringence of the waveplate could be varied to provide the polarization bias necessary for the polarizer to select the nonlinear polarization-rotated portion of the pulse. A Faraday mirror was placed at the end of the linear arm for reflecting light. In 1997, this sigma laser was utilized by Jones et al.<sup>[43]</sup> to generate a stretched-pulse fiber laser with a pulse duration of 104 fs. Tamura et al.<sup>[44]</sup> mentioned that self-starting from noise is very difficult to achieve in a linear cavity, and harder in a Fo8 or sigma cavities that use fast SA because of the weak pulse-shortening strength for long pulses. In a linear cavity proposed by Haus et al.,<sup>[45]</sup> reflections create a multiple Fabry–Perot structure with unevenly spaced resonant modes. The fast SA should injection lock these uneven modes to an evenly spaced set of oscillating modes to achieve mode-locking. However, spurious reflection creates injection signals that pull the mode frequencies (mode pulling) away from the desired even spacing, which prohibits the mode-locking if the SA signal is weak. A unidirectional ring cavity employing an isolator facilitates self-starting by minimizing étalon effects and counter-propagating waves in the linear cavity. Since the self-starting condition ( $\kappa NP$ ) has a less harsh condition of only one surface of reflectance ( $r_i$ ) for the ring cavity rather than higher order ( $r_i r_j$ ) for the linear cavity, where  $r_j$  is the second surface of reflectance, the self-starting of ring cavity is relatively easier and achievable than the linear cavity.<sup>[44,45]</sup>

The initiation of mode-locking in a linear, Fo8, or sigma laser cavities can be achieved using a starting trigger, e.g. using active mode-lockers, designing asymmetrical coupler ratios of a Fo8 cavity with additional mechanical perturbation or tapping. The Fo9 employs a modified cavity structure as compared with the Fo8 laser cavity, which makes the initiation of mode-locking more easily based on nonlinear phase bias. For instance, a non-reciprocal phase shifter is inserted in the main loop or the linear arm of the Fo9 laser cavity to introduce the phase bias.<sup>[29,46–48]</sup> The phase bias increases the transmission level of the running continuous wave and noise pulse at the starting point of the laser.<sup>[35,39]</sup> In this way, the transmission of light with low intensity is enhanced and the nonlinear transmission of loop mirror is shifted into peak power sensitive region, thus decreasing the mode-locking threshold. The self-start mode-locking ability was investigated by introducing a non-reciprocal phase shifter in the NOLM loop by a proper arrangement of Faraday rotators and waveplates.<sup>[29,47]</sup> The most common phase bias to shift the transmission is  $-\pi/2$ .<sup>[49]</sup> The effect of different phase bias values on the mode-locking threshold and phase noise was investigated, while the lowest mode-locking threshold and the highest phase noise value were obtained at the phase bias of  $-\pi/2$ .<sup>[50]</sup> Sometimes, self-start mode-locking is achievable without inserting the non-reciprocal phase shifter at the expense of higher

pump power threshold.<sup>[51]</sup> In contrast to Fo8 laser cavity, the Fo9 laser cavity offers several advantages, which include a simpler structure with fewer fiber components, minimized risk of optical damage, and higher average output power.<sup>[52,53]</sup> Hence, the Fo9 laser cavity often shows a higher laser slope efficiency and higher pulse energy than the Fo8 laser cavity, meanwhile simplifying the laser setup and reducing the cost of the laser system.<sup>[54]</sup> The Fo9 is feasible to operate either in transmission or reflection schemes. The MLFL with a reflective scheme was demonstrated by Menlo Systems GmbH under the trademark figure9<sup>TM</sup>. In contrast to a mirror loop which operates in a transmission scheme, a reflective mirror loop shows reduced maximum transmission when a larger asymmetrical coupling ratio is used at the junction. The accumulation of nonlinear phase shift by a non-reciprocal phase shifter prevents the utilization of a long optical fiber, which generates femtosecond laser pulses with a high repetition rate and a low noise,<sup>[29,55]</sup> that could meet the condition for practical applications such as space-borne frequency comb metrology.<sup>[56]</sup> Another practical application of picosecond MLFL generated from the Fo9 laser cavity is high-speed hyperspectral stimulated Raman scattering (SRS) microscopy.<sup>[53]</sup> The 3-dB tunability of more than  $280 \text{ cm}^{-1}$  which covers the entire CH-stretching region from  $2850$  to  $3050 \text{ cm}^{-1}$ , together with a spectral density of more than  $2 \text{ mW nm}^{-1}$  and average power of more than  $120 \text{ mW}$  are suitable for high-speed SRS imaging.

In this review, we discuss the differences between Fo8 and Fo9 laser cavity, as well as the pulse formation mechanisms, cavity optimization methods, and experimental setup of the Fo9 laser cavity. The Fo9 laser cavity has been employed to generate ultrafast and rectangular pulses in MLFLs. The current issues and challenges of the Fo9 laser cavity were outlined, along with some recommendations for future research directions. This review is anticipated to bring better insight into this laser structure for nonlinear optics, especially in pulse formation of the mode-locking regime.

## 2. The Fo9 Laser Cavity

This section began with a discussion on the pulse formation of a passively mode-locking regime. Next, the Fo8 and Fo9 laser cavities were compared in a comprehensive manner. The main difference between the two laser cavities occurs in the mirror loop. The Fo8 laser cavity exhibits a unidirectional mirror loop using an isolator, whereas the Fo9 laser cavity consists of a linear mirror arm using a high-reflective mirror. The Fo9 laser cavity has a relatively higher optical power than the Fo8 laser cavity because a larger portion of the average power circulating in the mirror loop of the Fo8 laser cavity is absorbed by the isolator. In the following sections, we discuss the difference in the roundtrip transmission curve versus nonlinear phase shift difference ( $\Delta\phi_{NL}$ ) between the Fo8 and Fo9 laser cavities, where phase bias ( $\Delta\phi_0$ ) of  $\pi/2$  and  $-\pi/2$  was employed for the Fo8 and Fo9 laser cavities, respectively to tune the increasing intensity and assist the self-start mode-locking operation. Next, we focus on the investigations for the optimization of the Fo9 laser cavity in terms of linear phase shift ( $\phi_L$ ), coupler splitting ratio, and fiber asymmetry of the NALM. In general,  $\phi_L$  of  $\approx 1.5 \pi$  makes the self-start mode-locking operation more easily, a coupler splitting ratio of 0.5 achieves the largest modulation depth that

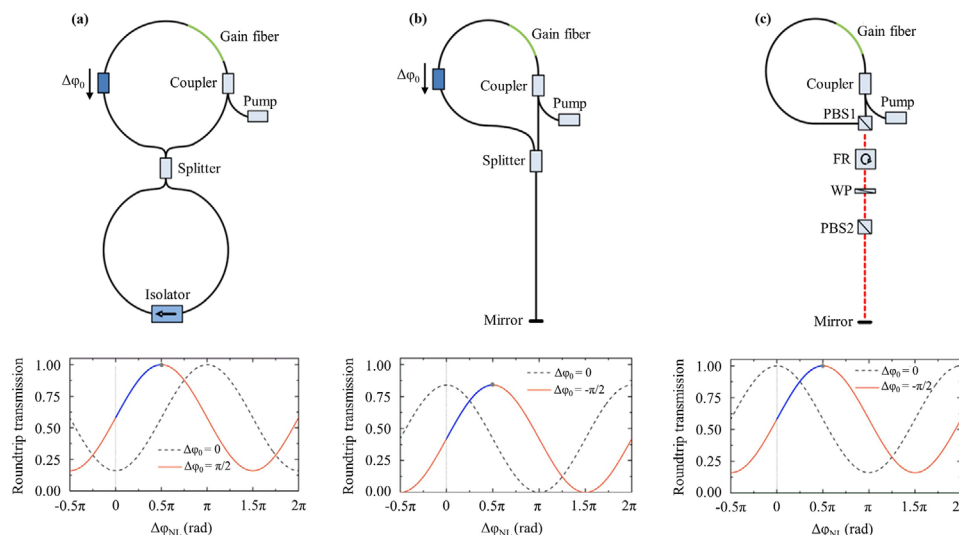


**Figure 1.** Schematic diagram of a) the Fo8 laser cavity, and the Fo9 laser cavities with b) a reciprocal and c) a non-reciprocal beam splitter. Reproduced with permission.<sup>[35]</sup> Copyright 2017, Springer.

generates higher output power and wider spectral bandwidth, whereas larger fiber asymmetry contributes to higher output power and  $\Delta\varphi_{NL}$ , thus reducing the threshold of self-start mode-locking operation. Finally, we elaborate the schematic diagram of Fo9 laser cavities of our previous experiment works in the operating wavelengths of  $\approx 1.0$ ,  $\approx 1.3$ ,  $\approx 1.55$ , and  $\approx 1.7$   $\mu\text{m}$ , for which the pulse formation was induced by the use of a non-reciprocal phase shifter, a graphene-microfiber and a section of long single-mode fiber.

## 2.1. Pulse Formation in the Passively Mode-Locking Regime

A passively mode-locking (ML) regime can be generated with saturable absorption. Saturable absorption is a nonlinear optical phenomenon that exhibits reduced optical loss at high optical intensity. At low optical intensity, the SA absorbs a high proportion of light and results in high optical loss. When the optical intensity is increased, the available energy states become depleted, leading to a reduction in absorption. When an intrinsic, material-based, or artificial SA is incorporated into a mode-locked laser cavity, the saturable absorption process initiates from inherent noise fluctuations of a laser cavity. This pulse initiation dynamic was studied with time-stretched dispersive Fourier transformation, where the original work was conducted by T. Jansson in 1983,<sup>[57]</sup> and comprehensively studied by Herink et al.<sup>[58–60]</sup> A dominant noise spike with the highest intensity will saturate the absorber and decrease the absorption loss. Next, the dominant noise spike is amplified in successive round-trips until a stable pulse train is eventually formed. This process favors the generation of laser pulses over continuous wave laser operation. In addition, a polarization controller or a set of waveplates is necessary in a non-PM laser cavity, which is used to adjust to the polarization state such that the maximum transmission or minimum optical loss at the polarizer occurs for the highest possible optical intensity. Subsequently, this configuration serves as an artificial SA, e.g., Fo8 and Fo9 laser, to generate the passively mode-locking regime.

## 2.2. Comparison Between Fo8 and Fo9 Laser Configuration

The operation of a Fo8 laser cavity could be mode-locked with either NALM or NOLM mechanisms,<sup>[33,34]</sup> whereas the first Fo9 laser cavity was demonstrated with a sigma laser using the NPE mechanism.<sup>[42]</sup> The NALM and NOLM mechanisms were also applicable for the Fo9 laser cavities using a phase shifter or a section of long single-mode fiber to provide asymmetrical gain.<sup>[61–64]</sup> Figure 1a shows the schematic diagram of a Fo8 laser cavity where the mirror loop is operated in a transmission manner, while Figure 1b,c represents the schematic diagram of a Fo9 laser cavity with a reflective mirror loop in the linear arm configuration.<sup>[35]</sup> It is feasible for the Fo9 laser cavity to adapt a phase shifter that induces reciprocal or non-reciprocal phase biases. Self-start mode-locking is achieved by optimizing phase biases, which also provide highly efficient reflection into the linear arm at favorable operational conditions. Furthermore, there is no restriction on the application of a phase shifter in the NALM of the Fo8 laser cavity. Instead of using a phase shifter, the NALM of the Fo8 laser cavity can also work on the phase shift between laser pulses that are first amplified and then propagated in the long passive fiber, which then traveling the opposite way around. As a result, the laser pulses experience stronger intensity-dependent nonlinearity during the roundtrip. When the nonlinear phase difference or input pulse intensity increases, the transmission of the NALM increases, thus acting as an artificial SA. In the experimental setup, an obvious difference between the Fo8 and Fo9 laser cavities occurs at the mirror loop. In the Fo8 laser cavity, a  $2 \times 2$  coupler splits the outputs which are connected through an isolator, thus leading to a unidirectional mirror loop. This method shows a disadvantage because a great portion of the average power circulates in the forbidden direction is absorbed by the isolating component, thus limiting the generation of high optical power, in practical. On the other hand, a Fo9 laser cavity shows an improved configuration compared to a Fo8 laser cavity by significantly simplifying the laser construction with fewer optical components. The mirror loop is reconstructed by disconnecting



the coupler exit ports. A reflecting component, such as a fiber mirror, fiber ferrule mirror, FR mirror, and bulk mirror, is coupled to one of the exit ports of the coupler. These mirrors ensure positive feedback is generated in the NALM, meanwhile allowing higher optical power to be fully recycled, measured, and utilized at another exit port of the coupler. In particular, the FR mirror was used in the original work of the sigma laser which works together with a Faraday rotator and waveplates to generate the NPE in the straight arm.<sup>[42]</sup> The NALM loops of both Fo8 and Fo9 could also be employed with a non-PM fiber that offers higher flexibility with an intrinsic non-reciprocal condition using polarization controllers.<sup>[25]</sup> On the other hand, the NALM loops incorporating PM fibers are strictly reciprocal for low intensity, unless an additional non-reciprocal phase shifter is incorporated into the Fo9 laser cavity, as shown in Figure 1c. Without introducing this non-reciprocal phase bias into the all-PM Fo9 fiber laser cavity, the transmission for low intensity remains constant, thus impeding the self-start mode-locking of the laser.<sup>[40,65]</sup>

The bottom column of Figure 1 shows the roundtrip transmission curve as a function of  $\Delta\varphi_{NL}$ . The Fo8 laser cavity illustrates an increasing in transmission, while the reflective variants show a decreasing in transmission as a function of  $\Delta\varphi_{NL}$ , denoted by the dashed line in the roundtrip transmission curve, assuming a splitting ratio of 0.7. An exemplary phase bias ( $\Delta\varphi_0$ ) of  $\pi/2$  and  $-\pi/2$  were used for the Fo8 and Fo9 laser cavities, respectively to tune the intensity (blue and red lines), thus supporting self-start mode-locking of the laser. The blue part of the round-trip transmission marks the evolution of the laser from continuous-wave to pulsed laser operation. The Fo9 laser cavity in Figure 1c exhibits the maximum transmission of 1, which is inherent to a Fo8 laser cavity. The non-reciprocal phase shifter generates this feature by combining a FR and a waveplate (WP), that were placed between two polarizing beam splitters (PBS1 and PBS2) to control the phase difference between the counter-propagating beams.<sup>[35]</sup> Sometimes, more FRs and WPs were used for the self-start mode-locking.<sup>[66,67]</sup> If the phase shifter consists of several adjustable WPs, both the phase bias and modulation depth can be adjusted to provide a tunable structure with optimized laser pulse operation. As shown in Figure 1c, the fiber between PBS1 and the linear mirror arm is twisted by  $90^\circ$  to ensure a complete transmission at the entrance and reflection from the exit of the linear mirror arm, respectively. Hence, the pulse propagation with a linear polarization of  $45^\circ$  will be reverted when passing through the FR. The phase shift of the WP is oriented at  $45^\circ$  which leads to a non-reciprocal phase bias of  $\Delta\varphi_0 = 2\Delta\varphi$  per round trip. The manipulation of the angular orientation of PBS2 or adding a half-waveplate in front of PBS2 can result in the deviation of the splitting ratio between the NALM and linear mirror arm from 0.5 without affecting the round-trip transmission of the laser. An advantage of Fo9 laser cavity is the feasibility of employing a reflective mirror. For instance, the graphene electro-optics modulator (GEOM) and a mirror with a piezo-transducer (PZT) can be integrated easily to achieve a high pulse repetition rate ( $f_r$ ).<sup>[29,68]</sup> In particular, the GEOM was installed for the fast control of carrier-envelope offset (CEO) frequency ( $f_{CEO}$ ) or  $f_r$  and beating frequency ( $f_{beat}$ ), whereas the PZT was attached to fiber for the slow control of  $f_{beat}$  or  $f_r$ .

### 2.3. Optimization of the Fo9 Laser Cavity

The ability to self-start a mode-locked laser was studied in terms of the value of  $\varphi_L$  introduced to a Fo9 laser cavity with a given cavity asymmetry.<sup>[1,35]</sup> In particular, an optimized  $\varphi_L$  introduced in the ring mirror or the linear arm of the Fo9 cavity increases the transmission level of the running CW laser and noise pulse at the laser starting point.<sup>[69]</sup> This generates the initial noise-like giant pulses required to enhance the self-starting ability of the mode-locking. As a result, the mode-locking threshold is reduced and the self-starting becomes simpler. The mechanism of pulse formation in a NALM depends on the disproportion of phase shift accumulated by pulse propagation through the gain medium in opposite directions. Figure 2 illustrates the transmission curve of the Fo9 laser cavity as a function of nonlinear phase shift ( $\varphi_{NL}$ ). The relationship between  $\varphi_{NL}$  and transmission denotes the splitting ratio of 0.5 and gain of 1 in the equivalent NALM for different  $\varphi_L$ . The difference in  $\varphi_L$  generates a range corresponding to single-pulse mode-locking operation where the transmission of the pulse is larger than that of continuous wave components, which is indicated in the thickened part in Figure 2. The  $\varphi_L$  of  $1.5\pi$  is optimal for generating self-start mode-locking due to its largest slope at the low-power region of the transmission curve. On the other hand, the self-start mode-locking becomes more difficult for a smaller  $\varphi_L$  due to the smaller slope at the low-power region of the transmission curve. Moreover, a larger nonlinear phase shift difference ( $\Delta\varphi_{NL}$ ) is required to self-start mode-locking when the value of  $\varphi_L$  becomes smaller. While having an excellent self-start mode-locking function by setting  $\varphi_L$  to be  $\approx 1.5\pi$ , the pulse energy of the Fo9 laser cavity can also be enhanced. By gradually reducing the  $\varphi_L$  from  $1.5\pi$  and increasing the laser pump power, the  $\Delta\varphi_{NL}$  is ensured to always stay within the region of single-pulse mode-locking operation, thus increasing the pulse energy of the Fo9 laser cavity. The red curve in Figure 2 denotes the self-start mode-locking operation of the Fo9 laser cavity at the initial  $\varphi_L$  stage. By gradually increasing the laser pump power, the laser can operate near Point A with single-pulse mode-locking pulse generation. By superimposing  $\varphi_L$  with a small increment of  $-\Delta\varphi_L$ , the transmission curve is highlighted by the purple curve in Figure 2. The reduction of  $\varphi_L$  leads to a right-shift of the transmission curve, thus increasing the peak power of the pulse. Meanwhile, the value of  $\Delta\varphi_{NL}$  is increased that shifts the laser to operate at Point B. Point B remains in the single-pulse mode-locking region if  $\Delta\varphi_{NL}$  is small. The increase in pump power could make the laser operate even at Point C within the maximum allowable  $\Delta\varphi_{NL}$ . By repeating the above process of reducing  $\varphi_L$  and increasing pump power, the operation point of the laser could move to Point D on the green curve and Point E on the black curve without affecting the self-start single-pulse mode-locking of the laser. As a result, the pulse energy of the Fo9 laser cavity could be greatly enhanced by the reduction of  $\varphi_L$ , whereas the self-start single-pulse mode-locking for the laser is maintained. The discussion in Figure 2 provides insight into the optimal  $\varphi_L$  within the maximum allowable  $\Delta\varphi_{NL}$ , where the pump power could be increased without affecting the single-pulse mode-locking operation of the laser. This is an important technique to increase the pulse energy of the Fo9 laser cavity because multiple-pulse mode-locking generates a higher pulse repetition rate, thus causing a reduction of pulse energy.

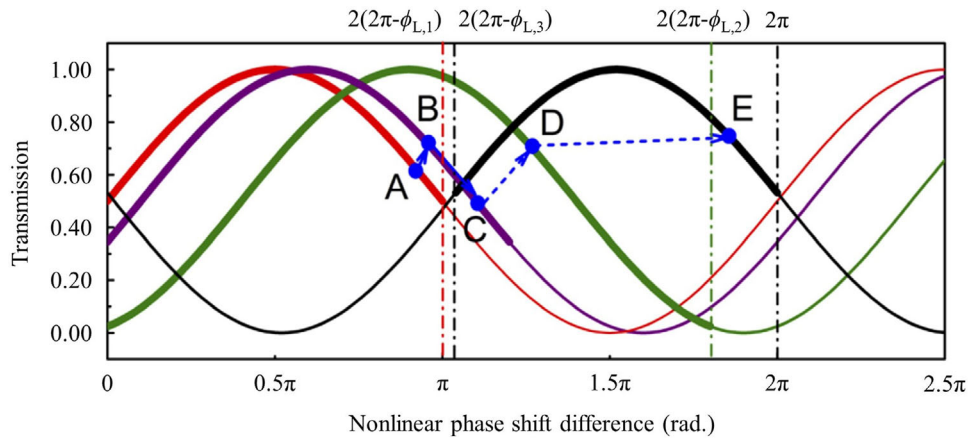


**Figure 2.** Transmission curves of the Fo9 laser cavity with different  $\phi_L$ . The  $\phi_L$  for the red, purple-green, and black curves are  $1.5\pi$ ,  $1.5\pi - \Delta\phi_L$ ,  $\pi$ , and  $0.5\pi$ , respectively.  $\Delta\phi_L$  denotes the linear phase shift difference. Reproduced with permission.<sup>[1]</sup> Copyright 2020, Optica.

Apart from understanding the effect of  $\phi_L$  for self-start mode-locking, the influence of the splitting ratio of the  $2 \times 2$  optical coupler connecting the NOLM or NALM to the mirror loop of a Fo9 laser cavity was also investigated.<sup>[70]</sup> In the simulation, the parameters of non-reciprocal phase shift and bandwidth of chirped fiber Bragg grating were fixed to be  $0.5\pi$  and 20 nm, respectively. Based on **Figure 3**, the splitting ratio influences the modulation depth (MD) of the Fo9 laser cavity. A large deviation of the splitting ratio from 0.5 denotes a decrease in MD. A large splitting ratio results in a large asymmetrical power propagation at either the CW or the CCW direction which leads to a large  $\Delta\phi_{NL}$  between the counter-propagating beams. The large  $\Delta\phi_{NL}$  leads to a deterioration in both output power and spectral bandwidth when the splitting ratio is between 0.6 to 0.8. A double pulsing operation is generated when the splitting ratio is 0.4, whereas mode-locking is lost when the splitting ratio is less than 0.4 or more than 0.8. On the other hand, the highest output power and widest spectral bandwidth are attained when the largest modulation depth is achieved using the splitting ratio of 0.5. The investigation on the influence of different splitting ratios is important for the selection of an appropriate optical coupler for the Fo9 laser cavity, which can generate the highest laser output power at the largest modulation depth using a splitting ratio of 0.5.

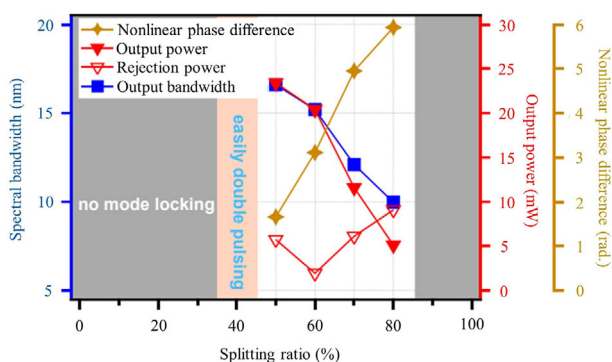


**Figure 3.** Influence of the  $2 \times 2$  coupler splitting ratio on the performance of the Fo9 laser cavity. Reproduced with permission.<sup>[70]</sup> Copyright 2021, IEEE.

The Fo9 laser cavity operates on  $\Delta\phi_{NL}$  between counter-propagating beams, which is typically achieved through asymmetrical passive fiber lengths,  $L_1$  for shorter length and  $L_2$  for longer length at both ends of the gain fiber inside the NALM loop. The length of  $L_1$  is fixed at 0.5 m. The reduction of  $L_2$  increases the NALM symmetry which alters the net dispersion and repetition rate of the laser cavity. In the simulation, laser cavity asymmetry was increased by increasing  $L_2$ , and the parameters of non-reciprocal phase shift and bandwidth of chirped fiber Bragg grating were fixed to be  $0.5\pi$  and 20 nm, respectively. The net dispersion and repetition rate of the laser cavity remained constant by simultaneously modifying the fiber length at the linear arm (mirror loop) accordingly. Based on the simulation result presented in **Figure 4**, the output power and  $\Delta\phi_{NL}$  increases, whereas the threshold of double-pulsing decreases at a larger fiber asymmetry. The mode-locking operation was not observed when  $L_2$  is shorter than 0.5 m. This result is important as it shows an optimum  $L_2$  ( $\approx 0.6$  m) with a high symmetrical length of  $L_1$  and  $L_2$  of  $\approx 0.5$ – $0.6$  m could maintain the mode-locking operation at the single-pulse state at the highest double pulsing pump power threshold. If a higher output power is desired, a longer  $L_2$  ( $\approx 2.0$  m) would be a wise choice.

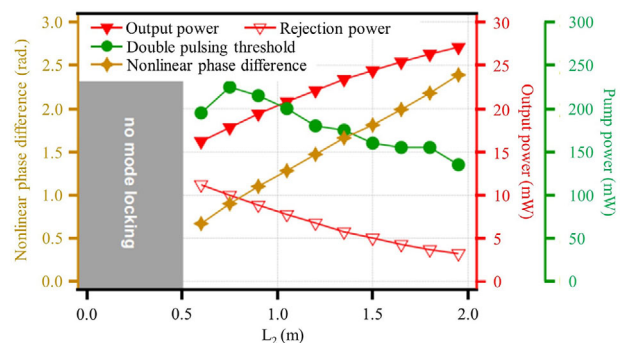


**Figure 4.** Influence of fiber asymmetry on the performance of the Fo9 laser cavity. Reproduced with permission.<sup>[70]</sup> Copyright 2021, IEEE.

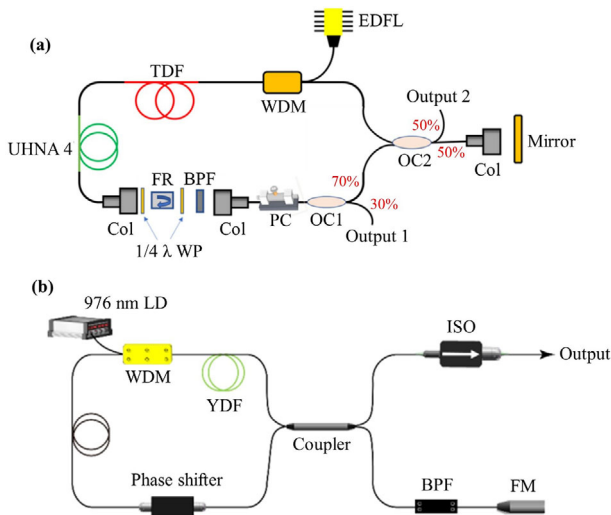


**Figure 5.** Schematic diagram of a) a 1.7  $\mu\text{m}$  Fo9 thulium-doped MLFL and b) a 1.0  $\mu\text{m}$  all-PM Fo9 ytterbium-doped MLFL using non-reciprocal phase shifters. Reproduced with permission.<sup>[62,72]</sup> Copyright 2022, Optica.

## 2.4. Experimental Setup of the Fo9 Laser Cavity

An example of our previous work of the Fo9 laser cavity using a non-reciprocal phase shifter constructed from two quarter-waveplates ( $1/4 \lambda$ ) and a FR for a thulium-doped MLFL operating at the wavelength of  $\approx 1.7 \mu\text{m}$  is depicted in **Figure 5a**.<sup>[62]</sup> The NALM and linear arm were connected via a  $2 \times 2$  optical coupler (OC2) with a splitting ratio of 0.5. The splitting ratio can be varied to 0.75:0.25.<sup>[71]</sup> A section of 0.7 m long thulium-doped fiber (TDF) was chosen as the gain medium, which is core-pumped by an erbium-doped fiber laser (EDFL) through a wavelength division multiplexer (WDM) with reduced reabsorption effect. A section of 2.9 m ultrahigh numerical aperture (UHNA 4) fiber was incorporated for dispersion compensation. A non-reciprocal phase shifter composed of a FR and two quarter-waveplates ( $1/4 \lambda$  WP) was utilized to control the  $\Delta\phi_L$  between the counter-propagating beams in the NALM, which was placed between two collimators (Col).<sup>[4]</sup> A phase shifter was used to initiate saturable absorption for the intra-cavity pulses.<sup>[6]</sup> When the phase shifter was removed, the intra-cavity pulse evolves into a reverse saturable absorption regime that avoids positive feedback of mode-locking operation.<sup>[35]</sup> The amplified spontaneous emission (ASE) at wavelengths longer than 1734 nm was suppressed by a band-pass filter (BPF) with a 3-dB bandwidth of 25 nm. A polarization controller (PC) is incorporated to tune the polarization state of the propagating light in different polarization angles and to improve the stability of the mode-locked laser. The spectrum without ASE was measured at Output 1 through a  $1 \times 2$  30/70 optical coupler (OC1). The reflective arm is made up of a gold-plated mirror with a reflectivity of  $\approx 100\%$ . The non-reciprocal phase shifter could also be constructed in a compact optical component consisting of a FR, a WP, and a reflective mirror as demonstrated in our previous work.<sup>[72]</sup> This non-reciprocal phase shifter enables MLFL operation in an all-PM laser design. The experimental setup of this all-PM ytterbium-doped MLFL is presented in **Figure 5b**. The ytterbium-doped fiber (YDF) was core-pumped by

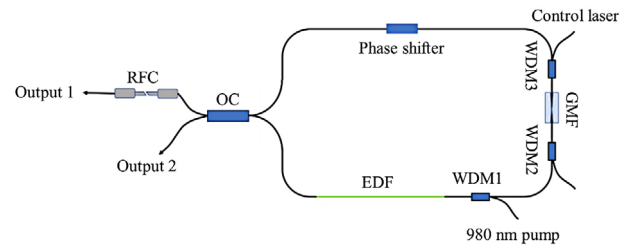


**Figure 6.** Schematic diagram of a 1.55  $\mu\text{m}$  Fo9 erbium-doped MLFL using a non-reciprocal phase shifter assisted by the GMF. Reproduced with permission.<sup>[63]</sup> Copyright 2022, Optica.

a 976 nm laser diode (LD), and the NALM was connected to the linear mirror arm via a coupler with a splitting ratio of 0.4:0.6. The isolator (ISO) was used to output the laser pulses, the high-reflective fiber mirror (FM) provides positive feedback to form the laser resonator, whereas the BPF with a center wavelength of 1030 nm and 3-dB bandwidth of 11 nm is employed to facilitate dissipative soliton mode-locking in all-normal dispersion regime. The all-PM design is very important for several practical applications. For instance, an all-PM erbium-doped fiber laser was demonstrated with excellent stability against accelerations in a rocket launching process although a PBS and two WPs were adopted to tune intra-cavity non-reciprocal phase shift.<sup>[56]</sup> Therefore, the adoption of all-fiber components, e.g., the experimental setup shown in **Figure 5b** can simplify the laser structure, which significantly improves the laser stability and eliminates uncertainty and tediousness during adjustments of PC or WPs. The packaging of the PBS, FR, and WP into a phase shifter component was also demonstrated in refs.<sup>[70, 73, 74]</sup> The packaging of multiple components into an phase shifter is an excellent technique to reduce the total cavity length, in particular, to decrease the bulkiness of the laser system and to increase the pulse repetition rate. However, a disadvantage of using this phase shifter is that this device is typically designed for the PM configuration, which might not be user-friendly for the non-PM laser cavity.

Besides providing phase bias using a non-reciprocal phase shifter, a graphene-decorated microfiber (GMF) was utilized to induce thermal nonlinearity to dynamically control the phase shift difference in a Fo9 erbium-doped MLFL cavity.<sup>[63]</sup> The schematic diagram of the laser cavity is given in **Figure 6**. A section of 6.1 m erbium-doped fiber (EDF) is core-pumped by a 976 nm LD through WDM1. The GMF is inserted between WDM2 and WDM3 to provide unequal intensity of counter-propagating beams. Therefore, a higher  $\Delta\phi_{NL}$  could be attained by controlling the laser power of the GMF. The incorporation of a non-reciprocal phase shifter provides a phase bias to the roundtrip transmission curve which contributes to the saturable absorption effect on the laser cavity. Nevertheless, the  $\Delta\phi_{NL}$  might be limited by the available pump power in the experiment for self-start mode-locking operation. Hence, the GMF was incorporated as an external control to increase the transmission rate, thus reducing the threshold of self-start mode-locking operation. In the experiment, the mode-locking pump power threshold was recorded to be 390 mW and from 300 to 390 mW, without and with the GMF, respectively. The  $2 \times 2$  optical coupler (OC) has a splitting ratio of 0.45:0.55, whereas the linear arm comprises a 90% reflective FC/PC connector (RFC). The Output 1 and Output

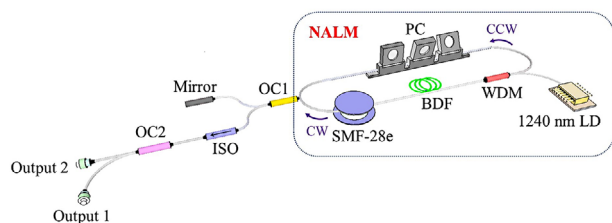


**Figure 7.** Schematic diagram of a 1.3  $\mu\text{m}$  Fo9 bismuth-doped MLFL using SMF-28e. Reproduced with permission.<sup>[64]</sup> Copyright 2023, IEEE.

2 allow for simultaneous measurement for output and rejected laser signals, respectively.

Apart from introducing phase bias with a non-reciprocal phase shifter and increasing transmission at the optimum  $\Delta\phi_{\text{NL}}$  with the GMF, we developed a 1.3  $\mu\text{m}$  Fo9 bismuth-doped MLFL using a section of  $\approx 950$  m long spool of standard single-mode fiber (SMF-28e) with a dispersion of  $-0.021 \text{ ps}^2 \text{ m}^{-1}$  to provide asymmetrical gain for the CW and CCW laser lights in the bidirectional NALM loop as shown in Figure 7.<sup>[64]</sup> The optical fibers, e.g., SMF-28e<sup>[5,54]</sup> and highly nonlinear optical fibers<sup>[75,76]</sup> could be employed to introduce the Kerr nonlinear effect in the laser cavity.<sup>[77]</sup> The Kerr nonlinear effect exhibits minor degradation of either peak or average power level inside the laser cavity, whereas the loop mirror is only limited by the reliability of the optical components.<sup>[78]</sup> Next, a section of 20 m bismuth-doped fiber (BDF) was core-pumped by a 1240 nm laser diode (LD) through a 1240/1310 nm WDM. The  $2 \times 2$  OC1 with a splitting ratio of 0.5 and a PC was employed to optimize the polarization state of propagating light in the Fo9 laser cavity. The linear arm consists of a fiber mirror with a reflectivity of  $\approx 95\%$ . This fiber mirror could also be replaced by a coupler with a splitting ratio of 0.5, where both output ports are spliced together. Assuming the coupler exhibits a similar splitting ratio, the loop mirror should act as an ideal mirror, reflecting the majority of the power entering the loop mirror back into the NALM.<sup>[33]</sup> At the other exit port of the  $2 \times 2$  OC1, an ISO was incorporated to prevent back-reflection of the output signal. The measurement was done simultaneously at Output 1 (95%) and Output 2 (5%) for laser signals through a  $1 \times 2$  OC2. The MLFL at  $\approx 1.3 \mu\text{m}$  is unique because rare-earth-doped materials do not have efficient emission at the second telecommunication window. This research was reported recently using a bismuth-doped phosphosilicate optical fiber to achieve a seed MLFL with a maximum pulse energy of  $\approx 200 \text{ nJ}$ .<sup>[64]</sup> Further investigation of bismuth-doped MLFL using Fo9 for achieving a higher pulse energy, a shorter pulse width, and a higher peak power is of high importance to meet the increasing demand of the MLFL for telecommunication applications.

### 3. Pico/Femtosecond MLFL

The Fo9 laser cavity was used to develop picosecond or femtosecond MLFL. In this section, the experimental parameters and the results of the ultrafast MLFL will be discussed. In the final subsection, a table of summary is provided to bring a clear insight on the MLFL performances that have been reported by using the Fo9 laser cavity in the near-infrared wavelength region.

### 3.1. Experimental Parameters

The experimental parameters can be studied in terms of their influence on the MLFL performance of a Fo9 laser cavity. These experimental parameters include net cavity dispersion which can be designed in either anomalous, dispersion-managed, near-zero in normal or normal regimes using a dispersion compensating element, polarization state which causes a deviation in phase shift between counter-propagating beams in the NALM, pump hysteresis which provides an insight on pump power zones where single or multi-pulse states occur, and the differences in optical spectra recorded from both output and reject ports of a Fo9 laser cavity.

#### 3.1.1. Net Cavity Dispersion

The management of net cavity dispersion provides different pulse formation mechanisms for mode-locking, such as soliton, dissipative soliton (DS), stretched-pulse, and soliton similariton.<sup>[79,80]</sup> The dispersion regimes for these mechanisms are anomalous, normal, dispersion-managed, and near-zero in normal regimes, respectively. For ytterbium-doped MLFL, typical net cavity dispersion is normal that works in the DS regime, unless a dispersion compensating element, e.g., a chirped fiber Bragg grating (CFBG) or a pair of grating, is applied. For instance, dispersion management was conducted from  $+0.019$  to  $-0.031 \text{ ps}^2$  for a ytterbium-doped MLFL using a CFBG.<sup>[74]</sup> The pulse width was recorded to be 5.5 ps without external compression by the CFBG. The CFBG provides the net anomalous cavity dispersion to the laser cavity, where the output pulse was characterized with 3-dB spectral bandwidth of 20.37 nm and pulse duration of 1.86 ps. The pulse width was compressed from 1.86 ps to 175 fs by a pair of grating with 600 lines  $\text{mm}^{-1}$ . In addition, the net cavity dispersion of an all-PM ytterbium-doped MLFL was compensated to  $0.01 \text{ ps}^2$  with a pair of gratings with 1000 lines  $\text{mm}^{-1}$ .<sup>[81]</sup> After pulse compression, the pulse width was recorded to be  $\approx 122 \text{ fs}$ . Apart from compensating the net cavity dispersion using the gratings, dispersion management of a ytterbium-doped MLFL can be made using a single-polarization large-mode-area photonics crystal fiber working at 1040 nm that manipulates the net cavity dispersion from  $-0.056$  to  $+0.002 \text{ ps}^2$  and reduces the pulse width from 199 to 68 fs.<sup>[82]</sup>

Apart from the ytterbium-doped MLFLs, there are several studies working on the net cavity dispersion management for an erbium-doped MLFL, where the laser cavity operates on an all-PM mechanism. For instance, the designs of soliton and stretched-pulse mechanisms were conducted with a net cavity dispersion of  $-0.0137$  and  $+0.0036 \text{ ps}^2$ , respectively.<sup>[28]</sup> In the stretched-pulse regime, an ultrashort pulse with a pulse width of 132 fs and a 3-dB spectral bandwidth of 46 nm was obtained. By designing the net cavity dispersion from  $-0.034 \text{ ps}^2$  to  $+0.006 \text{ ps}^2$ , the pulse width was reduced from 250 to 79 fs and the 3-dB spectral bandwidth was widened from 14 to 55 nm.<sup>[4]</sup> Moreover, the net cavity dispersion was investigated from  $-0.09 \text{ ps}^2$  for soliton to near-zero with micro-negative for stretched-pulse, which generates a pulse width from 360 to 96 fs, where the 3-dB bandwidth increases from 7.4 to 37.4 nm.<sup>[69]</sup> In another work, the pulse width reduced from 145.8 to 99.8 fs when net cavity



dispersion was measured from  $-0.021$  to  $-0.002$  ps<sup>2</sup>.<sup>[83]</sup> In addition, the net cavity dispersion was recorded from  $+0.023$  to  $+0.254$  ps<sup>2</sup> in the DS regime to generate three distinguishable operation states of the MLFL in terms of optical spectrum by increasing or decreasing the slit's aperture of the intracavity compressor at a constant power.<sup>[84]</sup> The 3-dB spectral width could be increased from 1.92 to 3.69 nm without losing the mode-locking operation. Apart from erbium-doped MLFL, a CFBG was incorporated to compensate for the anomalous dispersion of a thulium-doped MLFL.<sup>[85]</sup> The net cavity dispersion was measured to be  $-0.06$  ps<sup>2</sup> after dispersion compensation, which generates a pulse width of 449 fs. By incorporating an external amplifier, the output power was amplified from 2 to 20 mW and experienced a nonlinear pulse evolution process which compresses the pulse width to 123 fs due to the nonlinear compression effect during amplification. Up to the present, most studies demonstrated the net cavity dispersion compensation from anomalous to near-zero or normal, because the MLFL operating in both near-zero (stretched-pulse) and normal (dissipative soliton) dispersion regimes could achieve a shorter pulse width, by using just an external dispersion compensation scheme, e.g. a CFBG or pair of grating for the MLFL working in normal dispersion regime.

### 3.1.2. Polarization State and Pump Hysteresis

The tuning of the polarization state occurs in a non-PM Fo9 laser cavity, which can be done by either rotating the polarization controller or the WP angles, e.g., a non-PM mode-locked TDFL cavity in Figure 5a.<sup>[62]</sup> For instance, the rotation of the WPs within a phase bias device will deviate the phase shift between counter-propagating beams in the NALM.<sup>[46,62]</sup> A WP alters the polarization state of a traveling light wave by shifting the phase between two perpendicular polarization components of the light wave. The two perpendicular polarization components include the ordinary axis with index of refraction ( $n_o$ ) and the extraordinary axis with index of refraction ( $n_e$ ). The ordinary axis is perpendicular to the optical axis, whereas the extraordinary axis is parallel to the optical axis. For a light wave that incident upon the WP, the polarization components along the ordinary and extraordinary axes travel through the WP with a speed of  $c/n_o$  and  $c/n_e$ , respectively ( $c$  is the speed of light in vacuum). This leads to a phase difference between the two polarization components as they exit the WP. The WP is characterized by the amount of relative phase ( $\Gamma$ ), that it imparts on the two components, which is related to the birefringence ( $\Delta n$ ) and the thickness ( $L$ ) of the WP by the formula:

$$\Gamma = \frac{2\pi\Delta nL}{\lambda_0} \quad (2)$$

where  $\lambda_0$  is the vacuum wavelength of the light. The deviation in phase difference leads to a variation of the transmission curve against wavelength as shown in Figure 8. A bandpass filter with a center wavelength of 1734 nm and a 3-dB bandwidth of 25 nm was utilized in the laser cavity. The rotation of WP with three different angles allows for tuning of the 3-dB bandwidth of the MLFL from 7.5 to 20 nm and the tuning process is repeatable. A slight red or blue-shift with respect to the center wavelength of the MLFL spectrum was observed due to the wavelength drift

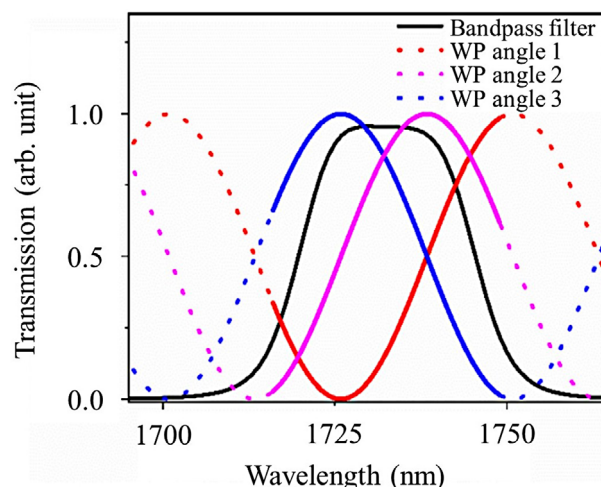


**Figure 8.** Transmission curves of the bandpass filter and MLFL spectra were recorded at three different WP angles. Reproduced with permission.<sup>[62]</sup> Copyright 2022, Optica.

corresponding to the highest transmission during the tuning process. Even though different 3-dB bandwidth was observed, the MLFL maintains a stable single-soliton operation at the expense of the output power.

The investigation of polarization state was performed by designing the half-waveplate (HWP) and quarter-waveplate (QWP) angles in a high-symmetry and a reduced-symmetry Fo9 laser cavity.<sup>[86]</sup> For the high-symmetry laser cavity, the accumulated  $\varphi_{NL}$  for the counter-propagating beams in the NALM has a negligible difference with  $L_1$  and  $L_2$  of 0.5 and 1.1 meters, respectively. The experimental parameters were set by the orientation of two WPs with a 3° step size at 400 mW pump power, and the pulsation states of the laser are depicted in Figure 9a. There are 64 areas that were circled where the Fo9 laser cavity presents high possibility of obtaining mode-locking operation. For the other WP angles, the Fo9 laser cavity forms either the Q-switched or continuous wave lasers. By reducing the symmetry of the Fo9 laser cavity with a splitting ratio of 0.65:0.35 at a step size of 3° and 200 mW pump power, the region shows relatively fewer areas where mode-locking operation is generated, as shown in Figure 9b. These studies of the influence of polarization states, e.g., different waveplate angles, on the MLFL could be highly useful for the design of a wavelength-switchable MLFL with different 3-dB bandwidths, and the change in the polarization state could also contribute to reduced pulse width with the 3-dB bandwidth getting larger. Moreover, the region where the laser operates in mode-locking, Q-switching, or continuous-wave laser could be accessed through the rotation of waveplate angles, which provides a comprehensive understanding of the pulse formation of mode-locked fiber laser.

Apart from rotating the waveplate angles and the polarization states, pump hysteresis is a phenomenon in passively MLFL which experiences the thresholds marking transitions between different pulsation states with increasing and decreasing pump power.<sup>[87,88]</sup> Pump hysteresis can occur in three different scenarios. 1) The mode-locking was initiated in multi-pulse state at a high pump power, which could enter the single-pulse state when

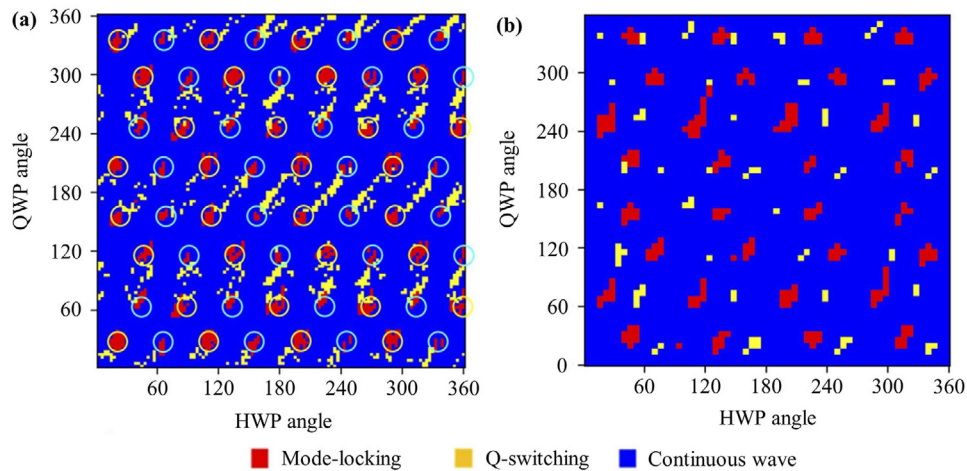


**Figure 9.** Experimental result for the Fo9 laser cavity with a) high-symmetry and b) reduced symmetry. Reproduced with permission.<sup>[86]</sup> Copyright 2022, Optica.

the pump power was reduced, 2) the mode-locking was initiated in multi-pulse state at a high pump power, which loses mode-locking operation when the pump power was reduced, 3) the mode-locking was initiated in single-pulse state at a high pump power, which maintains its single-pulse state when the pump power was reduced. Subsequently, the hysteresis effect is less obvious or even disappears as the fiber is cut shorter. A short cavity length contributes to a smaller deviation between  $L_1$  and  $L_2$ , based on Figure 4, thus leading to a higher possibility of a larger symmetry of a Fo9 laser cavity which accumulates the nonlinear phase shift difference that alternates between positive and negative values. The scenario allows the mode-locking operation of the Fo9 laser cavity to have both positive and negative phase biases.<sup>[86,89]</sup> The functionality of both positive and negative phase biases in a symmetry Fo9 laser cavity offers more hot-zones for mode-locking operation,<sup>[86]</sup> and supports a higher tendency of multi-pulse mode-locking state.<sup>[87]</sup> Therefore, the hysteresis effect is less obvious when the mode-locking has a higher tendency to be operated in the multi-pulse state. Due to the pump power hysteresis effect, the laser tends to obtain multiple pulse mode-locking at a high pump power.<sup>[86]</sup> If the pump power is tuned down, the single-pulse state can be achieved. In most scenarios, the mode-locked laser should be operated in a single-pulse regime for practical applications. The effect of cavity dispersion is important to increase the possibility of single-pulse operation. Li et al.<sup>[87]</sup> varied the cavity dispersion in the fiber loop by increasing the length of PM 2000D fiber which adjusts the dispersion from pure anomalous to normal dispersion regime, meanwhile, the total fiber loop length is kept constant by simultaneously adjusting the length of the PM 1550 fiber. In particular, the use of a longer PM 2000D fiber, e.g., the longest of 90-cm PM 2000D fiber, tends to provide a net normal cavity dispersion, which provides a higher tendency of mode-locking operation in the single-pulse state. The investigation of hysteresis dynamics was performed on a Fo9 laser cavity with high-symmetry using a 90-cm PM 2000D fiber, under 500 mW pump power and  $3^\circ$  step size as shown in Figure 10a. Figure 10b illustrates the hysteresis states in Region 1 of Figure 10a. There is a high proportion of pixels that can enter the single-pulse state. In particular, three yellow blocks ap-

pear which denotes the cavity can enter the single-pulse state directly. Figure 10c illustrates the hysteresis dynamics of each pixel, whereas the blue, red, and white parts indicate the pump power ranges for multi-pulse mode-locking (ML), single-pulse ML, and non-ML states, respectively. There are a large range of the pump power during the descent of pump power that maintaining single pulse mode (red cylindrical parts in Figure 10c), in conjunction with the red bars in Figure 10b. Moreover, the ratio of single-pulse state to total mode-locking state consisting of blue and red parts is depicted in Figure 10d. The optimization of a MLFL can be done by evaluating the mode-locking states based on this hysteresis-based scoring method,<sup>[90,91]</sup> as a larger single-pulse pump power range generally favors a higher mode-locking reliability. For example, a commercial laser needs four laser diodes to start pulse mode and needs only one to maintain single pulse. The interesting thing is that as the pulse repetition rate is increased to above 500 MHz, this mystery disappears.

In an all-PM thulium-doped MLFL, the pump power of 850 mW allows for a self-start mode-locking operation at  $\approx 1.7 \mu\text{m}$ , with proper rotation of the WPs.<sup>[62]</sup> The overdriven nonlinear effect caused by high pump power results in the multi-soliton regime of mode-locking operation. By virtue of pump hysteresis effect, the single-soliton operation was attained at a pump power of 350 mW as presented in Figure 11a. By increasing the pump power to 365 and 380 mW, the thulium-doped MLFL operates in double- and triple-soliton regimes, respectively. For triple-soliton regime, the intervals between generated solitons are not equally distributed along the laser cavity with a constant interval between primary pulses at 42.80 ns as shown in Figure 11b. These unequal intervals among the generated solitons can be tuned to be equal by carefully increasing the pump power and optimizing the polarization states through either a polarization controller or WP angles. The pump hysteresis was also employed to realize the stable mode-locking operation at a pump power of  $\approx 600$  mW, as compared with the high pump power of  $\approx 18$  W that produces unstable mode-locked laser pulses.<sup>[72]</sup> When the pump power was increased from  $\approx 1.5$  to 17.5 W, Q-switched laser pulses were generated due to the incorporation of a PS in the Fo9 laser cavity. In these reports, the study of pump hysteresis

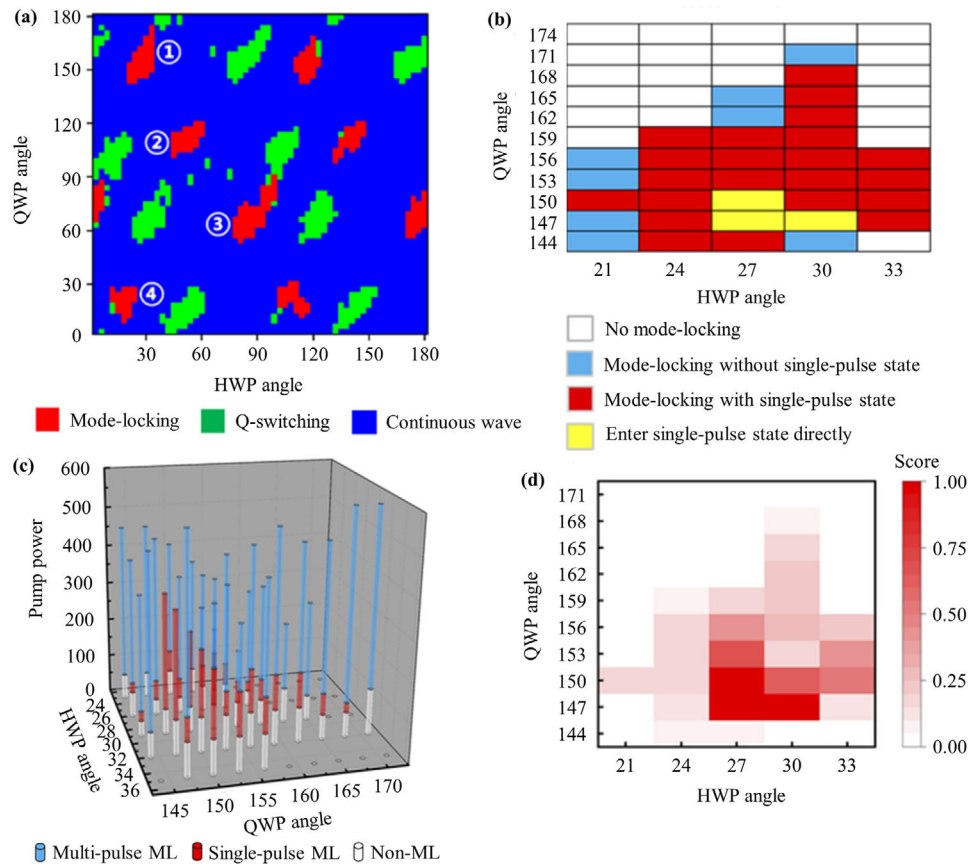


**Figure 10.** Experimental results for the Fo9 laser cavity with a high-symmetry using a 90-cm PM 2000D fiber, under 500 mW pump power and  $3^\circ$  step size. a) Mode-locking patterns obtained in experimental cavities and b) hysteresis states in Region 1 of Figure (a). c) Hysteresis of every pixel in Figure (b). d) Score of every pixel based on the ratio between single-pulse state and the whole mode-locking range in Figure (b). Reproduced with permission.<sup>[87]</sup> Copyright 2022, Optica.

provides a clear insight on that pump power range that enables single-pulse operation of mode-locked fiber lasers. For most scenarios, the mode-locked laser should be operated in a single-pulse regime for practical applications. The combined effect of optimizing the polarization states and pump hysteresis provides a better understanding of the pump power regions, where the non-ML, single-pulse or multi-pulse MLFL occurs, thus providing a clear selection rule of waveplate angles and pump power to achieve the desired operation scheme, e.g., single-pulse MLFL.

### 3.1.3. Output and Reject Ports

In the Fo9 laser cavity, output and reject ports are used to measure the MLFL. The output port is extracted through  $1 \times 2$  OC from the Fo9 laser cavity, whereas the reject port is the signal measured through the transmission of the reflective mirror arm, typically employing the CFBG. For instance, an investigation was carried out on the difference between output and reject ports of an all-PM thulium-doped Fo9 MLFL cavity.<sup>[49]</sup> It was found that

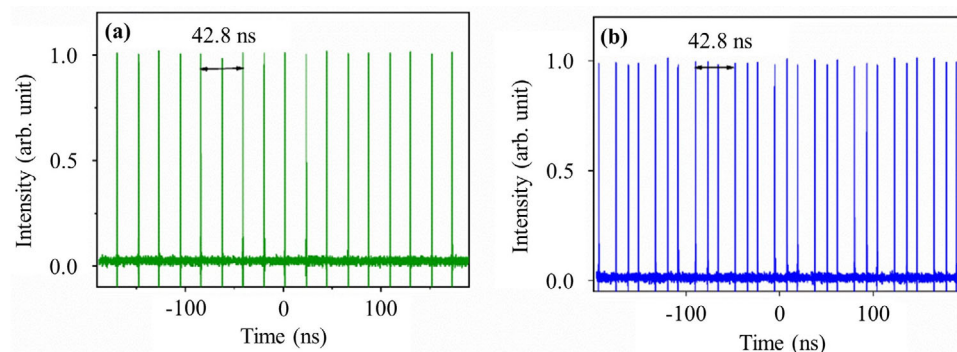


**Figure 11.** Pulse train of a) single-soliton pulse and b) triple-soliton pulse. Reproduced with permission.<sup>[62]</sup> Copyright 2022, Optica.

the Fo9 laser operates with repetition rate of 52.4 MHz and center wavelength of 1985 nm, with a 3-dB spectral bandwidth, pulse duration and pulse energy of 6.4 nm, 650 fs, 177 pJ for the output port and 19.2 nm, 1279 fs, 57 pJ for the reject port in the single-pulse state. The integrated relative intensity noise is over 3 times lower for the output port than that from the reject port, indicating that the output port has higher pulse quality. The investigation was also conducted for an erbium-doped MLFL working in soliton regime at a center wavelength of 1572 nm.<sup>[69]</sup> The 3-dB bandwidth and pulse width were measured to be 7.4 nm and 360 fs for the output port and 27.6 nm and 1.26 ps for the reject port, respectively. The reason for the larger pulse width even though the 3-dB spectral bandwidth is relatively wider at the reject port is due to the modulated optical spectrum. The reject port consists of radiation influenced by destructive interference, which causes spectrum sag and poor pulse quality. Besides, the differences between output and reject ports of the three operation states of an all-PM erbium-doped MLFL were analysed with regard to the influence of a set of operating parameters to the pulse characteristics.<sup>[84]</sup> The bandpass filter bandwidth is the key parameter to determine the achievable state of operation and the 3-dB spectral bandwidth of the laser pulses from 9.6 to 15.5 nm. Subsequently, the reject port could have comparable output performance to the output port. A CFBG incorporated ytterbium-doped MLFL operating at  $\approx 1030$  nm with net cavity dispersion of  $0.019 \text{ ps}^2$  was investigated in terms of its output and reject ports.<sup>[74]</sup> The pulse width was measured to be 3.2 and 5.5 ps for the output and reject ports, respectively. Moreover, the CFBG was also implemented into an all-PM ytterbium-doped Fo9 MLFL to provide large net cavity dispersion of  $-39.8 \text{ ps}^2$ , where the difference of its output and reject ports is compared.<sup>[92]</sup> The stable DS-MLFL operation is achieved at both output and reject ports with a close center wavelength, 3-dB spectral bandwidth, pulse width, repetition rate, and pulse energy of 1064.4 nm,  $\approx 0.16$  nm, 12.9 ps, 26.4 MHz and 3.5 nJ, respectively. From the discussed reports, the investigations on the role of output and reject ports provide a fair comparison where optimized experimental results were mostly observed at the output port rather than the reject port, e.g., larger 3-dB bandwidth, shorter pulse width, lower relative intensity noise, and higher pulse quality. Nevertheless, the simultaneous mode-locking operation was observed through the reject port, which might be useful for some practical implications with a lower requirement on mode-locked laser performance.

### 3.2. Experimental Result

Several experimental results of the MLFL generated through the Fo9 laser cavity was discussed. These experimental results include the generation of both Q-switched and mode-locked pulses, tunable MLFL that tends to be switched across a range of wavelengths, method and limitation to generate either high or low pulse repetition rates, noise suppression such as phase noise and intensity noise, as well as generation of the optical vortex beams. Finally, a table was presented which summarizes the previous MLFL works generated in the near-infrared wavelengths, mostly at  $\approx 1$ ,  $\approx 1.55$ , and  $\approx 1.7$  to  $2 \mu\text{m}$  based on the Fo9 laser cavity.

#### 3.2.1. Q-Switching and Mode-Locking

The Q-switching and mode-locking operations were observed in an all-PM ytterbium-doped fiber laser based on the Fo9 laser cavity.<sup>[72]</sup> First, the Q-switched laser pulses were observed at a pump power threshold of 1.5 W where the output power was measured to be 0.12 W. The repetition rate of the Q-switched laser pulses varied from 14.9 to 138.0 kHz and the pulse width reduced from 3900 to 970 ns, when the pump power was increased from 1.5 to 17.5 W. At the maximum pump power, the output power, pulse energy and peak power were measured to be 2.34 W, 17  $\mu\text{J}$  and 2 W, respectively. Owing to the fact that the intracavity peak power of a MLFL is typically hundreds of Watts or even higher,<sup>[93]</sup> the phase shifter incorporated into the Fo9 laser cavity drives the saturable absorption effect to achieve the Q-switching operation without employing strong nonlinear effects. By increasing the pump power to 18 W, the pulse train was instantly switched to an unstable pulsing at the fundamental repetition rate of the laser of 12.52 MHz. A comparison between Q-switching and mode-locking is that the repetition rate of Q-switched pulses increases with pump power, whereas mode-locked pulses show a constant repetition rate that corresponds to the laser cavity length. To realize stable mode-locking operation, the pump power was decreased to  $\approx 0.6$  W, which is lower than the threshold of the Q-switching by pump hysteresis effect. By increasing the pump power from  $\approx 0.6$  to 0.8 W, single-pulse mode-locking with a center wavelength of  $\approx 1030.16$  nm was generated, which shows output power from 36.5 to 56.3 mW, pulse energy from  $\approx 3$  to 4.5 nJ, pulse width from  $\approx 378$  to 500 fs, peak power from  $\approx 5.43$  to 9.76 kW, respectively after the laser pulse was dechirped and compressed by a pair of diffraction gratings with  $1000 \text{ lines mm}^{-1}$ . Apart from getting an insight on the pump power zones of laser operation schemes, the pump hysteresis is also important to achieve single-pulse mode-locking from a Q-switching laser regime by tuning down the pump power even below the Q-switching threshold. Mode-locking shows the main advantage of shorter pulse width than Q-switching laser regime, where the picosecond or shorter pulse width in mode-locking laser is very useful for practical applications such as laser welding and cutting with high precision.

#### 3.2.2. Wavelength-Switchable MLFL

A wavelength-switchable erbium-doped MLFL was demonstrated in a Fo9 laser cavity using galvanometer-driven intracavity filter.<sup>[94]</sup> The Fo9 laser cavity was constructed from a typical NALM and a non-reciprocal phase shifter, whereas the linear arm consists of a phase modulator and a wavelength-tunable intracavity filter comprising a collimator, a galvanometer scanner (GS) and a pair of diffraction gratings. The mode-locking operation is initiated with a pump power of  $\approx 150$  mW and by simultaneously applying a  $5 V_{\text{p-p}}$  radio frequency signal at  $\approx 27.5$  MHz to the phase modulator. The RF signal can be turned off after a stable pulse train is generated through mode-locking. Furthermore, under applying the RF signal and slightly increasing the pump power, the wavelength of the MLFL is switchable by rotating the direction of the GS in clockwise or anticlockwise manner. The wavelength is switchable from 1527 to 1559 nm, which



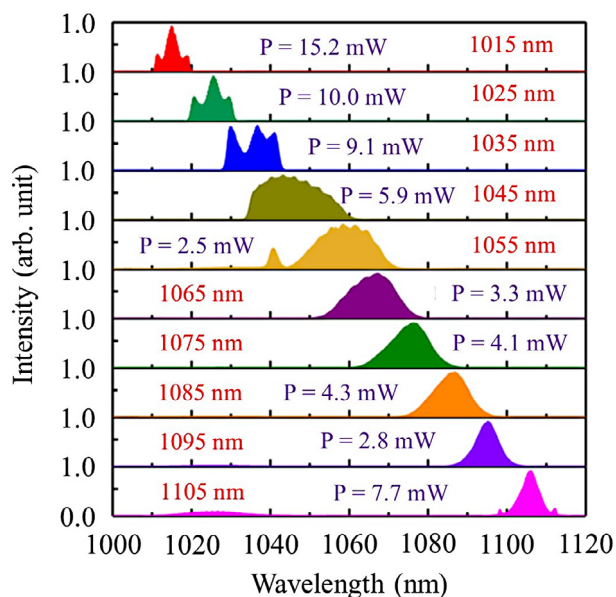


**Figure 12.** A switchable ytterbium-doped MLFL operating from 1015 to 1105 nm. Reproduced with permission.<sup>[96]</sup> Copyright 2022, Optica.

covers almost the entire C-band. The pulse width and 3-dB spectral bandwidth were recorded within a range from 1.1 to 1.7 ps and from 2.4 to 3.0 nm, respectively, whereas the pulse repetition rate is constant at 27.3 MHz. A similar work employing a Fo9 laser cavity consisting of a NALM, phase modulator and a diffraction grating for wavelength tuning was presented in ref.<sup>[95]</sup> The center wavelength, 3-dB spectral bandwidth and pulse width of an erbium-doped MLFL are switchable from 1525 to 1565 nm, 3.4 to 4.3 nm, 1.1 to 1.3 ps, respectively at a constant pulse repetition rate of 30.8 MHz by setting the pump power of  $\approx 100$  mW and applying a 10 V<sub>p-p</sub> radio frequency signal at  $\approx 30$  MHz to the phase modulator.

Besides, the Fo9 laser cavity was employed for an amplified ytterbium-doped MLFL, where the seed laser was generated from a Fo9 laser cavity, composed of a NALM, a phase modulator, and a grating pair for compensation of net cavity dispersion.<sup>[53]</sup> The seed and amplified signals present 3-dB spectral bandwidths of 5 and 45 nm, respectively. The amplified signal demonstrates a switchable MLFL operation from  $\approx 1010$  to 1050 nm. A larger tuning range from 1015 to 1105 nm was achieved in a ytterbium-doped MLFL by tilting the silver mirror behind the transmission grating pair as shown in Figure 12.<sup>[96]</sup> The output powers were recorded within a range of 2.8–15.2 mW. The net cavity dispersion is kept at near-zero dispersion between 0.0405 ps<sup>2</sup> at 1015 nm to  $-0.0221$  ps<sup>2</sup> at 1105 nm over the whole tuning range, which leads to the variation of the spectral shape. For instance, the optical spectrum centered at 1015 nm exhibits sharp peaks near the main band, corresponding to the hallmarks of dissipation generated in the net normal dispersion region. On the other hand, the observation of Kelly's sidebands of the optical spectrum centered at 1105 nm denotes the MLFL operates in the net anomalous dispersion region.

In another study, a significant wavelength redshift in the optical spectrum for MLFL pulses was observed owing to an increase

in pump power.<sup>[69]</sup> The increase in pump intensity contributes to an increase of  $\Delta\phi_{NL}$ , which causes the transmission versus wavelength curve to move toward long-wavelength direction. In addition, the rotation of half-WP angle in one direction leads to successive red-shifting and blue-shifting of the output spectrum. This wavelength shifting is due to the change in fast axis angle of the half-WP which leads to different transmission curve distribution of the output laser pulse. These wavelength-switchable MLFLs could provide a wider selection of wavelengths to meet the demands of various practical applications. Instead of designing multiple MLFL devices to offer the desired wavelengths, a wavelength-switchable MLFL decreases the bulkiness and complexity of the entire laser system, which can be achieved through the design of net cavity dispersion and optimization of polarization states by rotating waveplate angles.

### 3.2.3. Pulse Repetition Rate

The MLFL with a high pulse repetition rate is important in applications including optical arbitrary waveform generation, frequency metrology, ablation-cooled material removal and frequency comb.<sup>[97,98]</sup> The pulse repetition rate of a MLFL is directly influenced by the laser cavity length. Therefore, the reduction of laser cavity length, e.g., the total length of the incorporated fiber-based hybrid components consisting of WDM, PS and OC was demonstrated to generate fundamental pulse repetition of  $\approx 200$  MHz.<sup>[99]</sup> Apart from the fiber-based hybrid components, free space optical components such as a polarization beam splitter, and a phase bias consisting of FR and WP can further reduce the total laser cavity length, contributing to a relatively higher repetition rate up to 256.9,<sup>[100]</sup> 313,<sup>[101]</sup> 500.6,<sup>[102]</sup> and 700.1 MHz.<sup>[103]</sup> In comparison, the reduction of pulse repetition rate is limited by Q-switching instability and wave-breaking, even though the intracavity fiber length was increased in a Fo9 laser cavity working in narrowband DS-MLFL with periodically SA.<sup>[48]</sup> The Q-switching instability can be avoided by asymmetrically increase the passive fiber length in the NALM to lower the SA saturation power, leading to an effective reduction of repetition rate for laser pulses. Nevertheless, excessive reduction of SA saturation power might result in the generation of noise-like pulse (NLP), which restricts further reduction in repetition rate. To overcome NLP caused by excessive reduction of SA saturation power, increasing intracavity fiber length should be assisted by a periodic SA with non-reciprocal characteristics. The stabilization of pulse repetition rate with a low noise background is important for application in optical frequency combs.<sup>[29]</sup> The geometric length of the laser cavity is typically increased or decreased through mechanical motion to stabilize the pulse repetition rate. However, this method shows limitations in terms of high feedback voltage and mechanical disturbances attributed by piezoelectric ceramic transducer. To overcome these issues, the pump power can be controlled to regulate the refractive index of the gain fiber, thus stabilizing the pulse repetition rate in an optical manner.<sup>[104]</sup> For instance, the stabilization of repetition rate at  $\approx 80.1$  MHz was observed for 1 h with a standard deviation of 178  $\mu$ Hz within 1-s gate time. In addition, the control of pump power was used to study the influence of repetition rate that was locked at higher harmonic orders, e.g., 3th, 5th, and 10th harmonics, which were stabilized

with frequency fluctuation of 4.32, 2.42, and 1.19 mHz, respectively with suppression of phase noise. In these studies, the repetition rate is an important parameter that differentiates a pulsed laser, in particular, mode-locked laser from a Q-switched laser. To achieve an even higher (or a lower) pulse repetition based on typical mode-locking lasers to the few GHz level (or kHz level), various schemes should be considered, such as the method to further reduce the laser cavity length, and the restriction of Q-switching instability and wave-breaking to obtain shorter repetition rate below a few kHz.

### 3.2.4. Low-Noise Operation

According to Section 3.1.4, the output and reject ports in several Fo9 laser cavity designs were incorporated with reflective elements such as CFBG. The output and reject ports have different output laser features. For instance, by measuring the phase and intensity noises of these two output ports, the reject port is shown to have lower noise with a signal-to-noise ratio (SNR) of 95 dB in contrast to the output port with a SNR of 80 dB.<sup>[85]</sup> The high SNR at the reject port is attributed to the transmission properties of the NALM. The physical mechanism of noise suppression in a NALM can be studied using the model of an asymmetric Sagnac interferometer, where the transmission ( $T$ ) is related to nonlinear phase accumulation difference between two counter-propagation beams with a certain splitting ratio ( $\eta$ ).<sup>[33,85]</sup>

$$T = 1 - 2\eta(1 - \eta)[1 + \cos(\Delta\psi)] \quad (3)$$

where  $\Delta\psi$  is the difference of nonlinear phase shift,  $\psi_1$  and  $\psi_2$  accumulated by two counter-propagating beams are given as:

$$\Delta\psi = (1 - \eta)\psi_1 - \eta\psi_2 \quad (4)$$

The difference in nonlinear phase shift is determined by several factors such as the peak power of the pulses, effective mode area, and the effective length of the NALM. For instance, a fluctuation in peak power of the pulses ( $\Delta P$ ) causes a corresponding fluctuation in the nonlinear phase shift accumulation, where the transmission which was affected by peak power fluctuation ( $T_{\Delta P}$ ) is expressed as:<sup>[105]</sup>

$$T_{\Delta P} = T(P + \delta P) \quad (5)$$

where  $P$  and  $\delta P$  are the peak power at the initial and fluctuated stages, respectively. By designing the NALM with an asymmetric structure such that the nonlinear phase shift difference is positive and transmission with respect to peak power is negative, the amplitude noise of the intracavity pulse could be suppressed. **Figure 13** shows the evolution of transmission and reflection of the NALM loop as a function of nonlinear phase shift difference. A nonlinear phase shift difference of  $\approx 0.2\pi$  was identified, which corresponds to an operation regime with suppressed amplitude noise.

In an all-PM erbium-doped MLFL based on the Fo9 laser cavity, noise suppression was investigated with a fundamental repetition rate of up to 103.4 MHz.<sup>[106]</sup> A high SNR of 93.1 dB was recorded through the RF spectrum. Moreover, the stabilization of the pulse laser at the fundamental repetition rate was

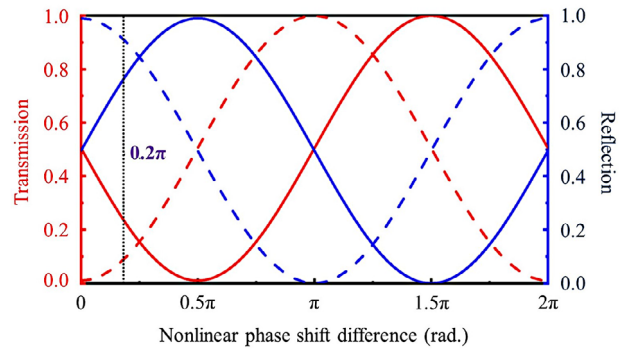


**Figure 13.** Transmission and reflection curves of the NALM loop against  $\Delta\psi$  with phase bias of  $\pi/2$  (solid line) and 0 (dashed line). Reproduced with permission.<sup>[85]</sup> Copyright 2023, IEEE.

achieved by using a frequency actuator with a frequency stability of  $2.1 \times 10^{-12}$  at 1-s gate time. The integrated amplitude noise was measured to be 0.0056% at the fundamental repetition rate with a timing jitter of 63.7 fs. Later, the performance of low-noise mode-locked fiber lasers progressed rapidly.<sup>[107,108]</sup> The increasing demand for mode-locked lasers in various fields of science and applications encourages the development of a laser source with high robustness, reliable, and low-noise operation. An all-PM Fo9 laser cavity is an ideal candidate for a plethora of applications, where “hands-off” mode-locking is desirable,<sup>[56]</sup> due to the high robustness and reproducible self-starting characteristic. The MLFL also creates interest as a source of low-noise optical frequency combs. The optical frequency combs are precise measurement tools, which have applications ranging from high-precision spectroscopy and metrology to time-domain quantum physics.<sup>[109–111]</sup> The stabilization of optical frequency combs is important to achieve the full potential of these measurement tools with low-noise operation. In particular, the stabilization of optical frequency combs has been conducted in terms of carrier-envelope offset frequency ( $f_{\text{CEO}}$ ) in the erbium-based and ytterbium-based fiber laser configurations.<sup>[29,3,112]</sup> In the erbium-based configuration, the obtained phase noise of phase-locked  $f_{\text{CEO}}$  was obtained as 0.16 rad using the Fo9 laser cavity due to lower intrinsic phase noise,<sup>[29]</sup> compared to all-PM frequency comb incorporated with a SESAM that achieves phase-locked  $f_{\text{CEO}}$  of 0.25 rad.<sup>[113]</sup> In a following study, the timing jitter of the all-PM erbium-based frequency combs was measured using the balanced optical cross-correlation (BOC) method, which enables the measurement of timing jitter up to attosecond.<sup>[114]</sup> The timing jitter of the frequency combs was measured to be  $\approx 40$  attosecond from 10 kHz to 10 MHz.<sup>[29]</sup> A balanced optical cross-correlator method was adopted to measure the timing jitter for the direct output of a NALM mode-locked EDFL without amplification and pulse compression.<sup>[115]</sup> The free-running root-mean-square timing jitter was measured to be 99.63 attosecond from 10 kHz to 1 MHz. Hutter and coworkers investigated the minimization of CEO linewidth by varying the intracavity dispersion and repetition rate.<sup>[3]</sup> A free-running linewidth of sub-kHz range of  $\approx 100$  THz and 3-kHz range in the entire spectrum all the way up to 300 THz was achieved, thus proving the remarkably low-noise operation of the frequency comb. Apart from that a ytterbium-based frequency comb was generated through an all-PM Fo9 laser

configuration, whereas the stabilization of  $f_{\text{CEO}}$  was achieved to be  $10^{-19}$  at 1 s averaging time, and the integrated phase noise was measured to be  $\approx 0.47$  rad from 2 MHz to 1 Hz. Besides that, an investigation was made into an all-PM ytterbium-doped MLFL with a reflective phase biasing in different dispersion regimes, which shows the dependency of intensity noise and free-running linewidth of the carrier-envelope-offset (CEO) on the net cavity dispersion.<sup>[89]</sup> The experiment shows that a near zero net cavity dispersion contributes to significant suppression of relative intensity noise to be 0.003% with reduced CEO linewidth of less than 10 kHz at integration of 1 s, by operating the laser around the center wavelength of 1075 nm, that is far from the spontaneous emission peak of ytterbium at  $\approx 1030$  nm. In our opinion, an excellent MLFL should exhibit low-noise operation. The effort to achieve higher SNR, low timing jitter, and low  $f_{\text{CEO}}$  is very important. For instance, a recent work reported the femtosecond frequency combs with the significant advance of free-running linewidth of  $f_{\text{CEO}}$  below 1-kHz over an ultrabroadband spectral range from  $\approx 141$  to 306 THz.<sup>[3]</sup> The discovery of distinct minima in CEO linewidth at specific pump powers of the MLFL is important to provide a systematic analysis of the frequency noise of  $f_{\text{CEO}}$  and various optical comb lines.

### 3.2.5. Optical Vortex Beam

In recent years, optical vortex beams (OVBS) have attracted growing attention due to the spatial structure in association with quantum OAM properties.<sup>[116]</sup> The OVBS are spatially structured beams with a helical phase front that can carry orbital angular momentum (OAM) with different topological charge number.<sup>[117]</sup> This beam is characterized by a topological charge, and found to carry an OAM of  $lh$  per photon, where  $l$  is the topological charge and  $h$  is the reduced Planck's constant. In the analytic expression, a helical phase front is usefully related to a phase term of  $\exp(il\theta)$  in the transverse plane, where  $\theta$  is the azimuthal coordinate of intertwined helices. As a result,  $l$  exhibits positive, negative, or zero values, which correspond to clockwise or counter-clockwise phase helices or a Gaussian beam, respectively. The OVBS have donut-shaped spatial profile where the center has zero intensity due to phase singularity as shown in **Figure 14**. **Figure 14a,b** illustrates the spiral interferograms for the  $\pm 1$  order OAM captured using the interferometry setup.<sup>[118]</sup> The counter-clockwise and clockwise spiral interferograms were observed in **Figure 14c,d**, which indicates the generation of  $\pm 1$  order OAM.

In a Fo9 erbium-doped MLFL, a first-ordered linearly polarized LP11 mode and OVBS emitted by connecting a broadband long-period fiber grating (BLPFG) were reported, which exhibited mode conversion with a 3-dB bandwidth of 160 nm and resonance dip with a contrast of 14 dB.<sup>[119]</sup> This BLPFG was fabricated when group velocities between core modes of LP01 and LP11 in the two-mode fiber (TMF) were matched. Therefore, the broadband mode conversion can be achieved at zero group velocity matching. The mode purity of the output LP11 is higher than 98%. Minor difference in temporal feature between LP01 and LP11 OVBS reveal that the BLPFG does not affect the stability of mode-locking with pulse repetition rate of  $\approx 40$  MHz and SNR of more than 65 dB. Currently, the research

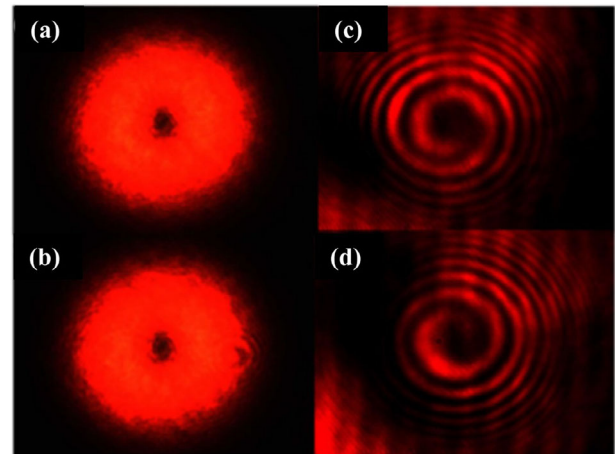


**Figure 14.** a,b) The intensity profiles of OAM $\pm 1$  mode; c,d) Corresponding spiral interferograms of OAM $\pm 1$ . Reproduced with permission.<sup>[117]</sup> Copyright 2022, IEEE.

on OVBS based on the Fo9 laser cavity is gaining growing attention, as compared to the aforementioned parameters such as wavelength-switchable MLFL, repetition rate, noise suppression, etc. These studies might open up a new research direction for mode-converter using ultrafast laser, especially to achieve different modes and phase fronts with higher mode purity and mode coupling efficiency.<sup>[120,121]</sup>

### 3.2.6. Summary

**Table 1** summarizes the MLFL seed sources generated through the Fo9 laser cavity. MLFLs operating at the three popular near-infrared wavelengths of  $\approx 1$ ,  $\approx 1.55$ , and  $\approx 1.7$  to 2  $\mu\text{m}$  were demonstrated due to the technical maturity and availability of active gain optical fibers, doped with ytterbium, erbium, and thulium/holmium, respectively. There are several remarkable examples listed in **Table 1**. For instance, a wavelength-switchable MLFL was presented from 1015 to 1105 nm,<sup>[96]</sup> few-mode MLFL was presented for LP01 and LP02,<sup>[119]</sup> pump current was used instead of pump power,<sup>[106]</sup> spectral bandwidth was measured as 10 dB instead of 3 dB,<sup>[122]</sup> and the implication of dual-pumping mechanism.<sup>[104]</sup>

## 4. Rectangular Pulse MLFL

From **Table 1**, the highest pulse energy of MLFL seed sources was reported to be  $\approx 4.5$  nJ.<sup>[72]</sup> The high pulse energy was achieved in an all-normal dispersion ytterbium-doped MLFL which can generate high pulse energy. Nevertheless, the requirement of large normal dispersion for a silica fiber and the complexity of manufacturing this expensive fiber avoids its large-scale application.<sup>[125]</sup> Besides, the high pump power and excessive nonlinear phase shift accumulated in the laser cavity can cause wave-breaking or pulse splitting for the intracavity pulses, which restricts the increase of pulse energy.<sup>[79,126]</sup> To overcome these problems, the implementation of high-gain fibers into a MLFL is beneficial to increase the output laser slope efficiency and thus

**Table 1.** MLFL seed sources generated with a Fo9 laser cavity.

$\lambda_c$ [nm]	$\Delta\lambda$ [nm]	$P_{\text{pump}}$ [mW]	$\tau$ [ps]	$f$ [MHz]	SNR [dB]	$P_{\text{out}}$ [mW]	$E_p$ [pJ]	$P_p$ [W]	Ref.
1015–1105	12–15	460	0.616–0.895	47.71 @ 1055 nm	94 @ 1055 nm	2.5–6.1	$\approx 52.4$ –127.85	85.06–142.85	[96]
$\approx 1028.7$	14.1	600	0.122	34.43	70	21	610	4850	[82]
$\approx 1030$	7.8	710	0.215	700.1	–	150	$\approx 215$	$\approx 1000$	[103]
$\approx 1030$	19	150	0.088	54.17	90	51	$\approx 941$	$\approx 7713$	[70]
1030.16	5.94	730	378	12.5	76	56.3	4500	9760	[72]
$\approx 1030.5$	20.37	190	1.86	47.3	70	12.13	260	$\approx 140$	[74]
$\approx 1040$	$\approx 24$	930	0.084	500.6	90	51	100	$\approx 855$	[102]
$\approx 1040$	$\approx 36$	1570	0.108	313	$\approx 45$	260	$\approx 520$	$\approx 4800$	[101]
1042	12.06	750	0.098	16.03	48	40.1	2500	25 000	[83]
1064.2	0.16	270	1) 10 2) 20	1) 1.7 2) 0.848	64	–	$\approx 40$ –100	$\approx 7$ –10	[48]
1064.4	0.17	550	12.9	26.4	75	91.9	3500	$\approx 271.3$	[92]
1529	11.9	70	1.2	17.78	62	0.62	34.87	$\approx 29.06$	[63]
1) 1546 (LP01) 2) 1560 (LP02)	1) 25 2) 15	70–125	1) 0.15 2) –	1) 34.270 2) 33.670	1) 70 2) 69	1) $\approx 0.5$ –2.5 2) $\approx 0.1$ –0.7	1) $\approx 14.6$ –73 2) $\approx 2.97$ –20.8	1) $\approx 97.3$ –486.7 2) –	[119]
$\approx 1550$	–	450–900	0.046	256.9	$\approx 55$	$\approx 75$ –104	$\approx 292$ –400	$\approx 6350$ –8700	[100]
$\approx 1558$	–	41	3.9	3.57	70	0.13	$\approx 36.4$	$\approx 9.3$	[41]
$\approx 1560$	46	500	132	44.9	65	$\approx 5$	$\approx 111.4$	0.84	[28]
$\approx 1560$	3.2–6.1	1000	1.92–3.69	$\approx 47.5$	$\approx 76$	2.4–14.48	150–280	159.5	[84]
1561.29	20.97	850	510	201.14	78	0.66	$\approx 3280$	6.43	[99]
1562	20.6	460 mA	0.189	103.4	93.1	6.82 @ 650 mA	65.96	$\approx 349$	[106]
1564	6.5	210	0.934	$\approx 5.2$	$\approx 50$	16.58	$\approx 3190$	$\approx 3415$	[123]
1564.3	20 @ 10 dB	220–380	6.73	55.6	80	16.3	290	$\approx 43$	[122]
1565	43	280	72	250	$\approx 80$	3	12	$\approx 0.17$	[35]
1569.5	17.6	LD1 = 135.1 LD2 = 34.5	1.83	80.1	60	5.22	65.17	35.6	[104]
$\approx 1570$	$\approx 55$	180	79	80.12	$\approx 65$	6.6	83	$\approx 1$	[4]
1571.65	18.7	504	0.477	121.03	80	$\approx 1.19$	$\approx 9.83$	$\approx 20.61$	[6]
1572	7.4	65	$\approx 360$	52	75	–	–	–	[69]
1573.2	41.6	136	0.093	59.3	70	5	$\approx 84.32$	$\approx 906.7$	[124]
$\approx 1575$	27	450	1.2	88.2	80	37	$\approx 420$	$\approx 350$	[50]
1726	7.5–20	350	4.08	23.36	$\approx 58$	0.35	15	$\approx 3.68$	[62]
1950	30	950	0.338	30.61	95	6.5	$\approx 212.3$	$\approx 628.1$	[85]
1985	6.4	405	0.65	52.4	–	$\approx 9.27$	177	$\approx 272.3$	[49]

$\lambda_c$  = center wavelength,  $\Delta\lambda$  = 3-dB spectral bandwidth,  $P_{\text{pump}}$  = pump power,  $\tau$  = pulse width,  $f$  = fundamental repetition rate, SNR = signal-to-noise ratio,  $P_{\text{out}}$  = output power,  $E_p$  = pulse energy,  $P_p$  = peak power, ref. = references, and LD = laser diode.

the pulse energy, but it leads to multi-pulsing instabilities (MPIs), such as soliton rain<sup>[127]</sup> and noise-like-pulse generation<sup>[128]</sup> at high operational powers. The MPIs and nonlinear-related distortion affect the achievable pulse intensities of soliton MLFLs, in which the fundamental limitation is caused by soliton area theorem.<sup>[129]</sup> In another work, a double-clad (DC) active fiber was employed to boost the output power and pulse energy of seed laser pulse in a chirped pulse amplification (CPA) scheme, which added significant complexity to the laser system.<sup>[130,131]</sup> Therefore, it remains highly demanded to design a MLFL seed source with a high pulse energy, simple laser cavity structure, cost-effectiveness, by utilization of conventional fiber, and minimizing the possibilities of MPIs and wave-breaking. Recently, the generation of high-energy rectangular pulse MLFL in a nanosecond time scale has been shown to exhibit these attractive fea-

tures which were developed in numerous applications, such as all-optical square-wave clocks,<sup>[132]</sup> laser micromachining,<sup>[133]</sup> and optical sensing.<sup>[134]</sup>

To circumvent the drawbacks of complex laser cavity configuration, the feasibility of generating high-energy pulses directly from MLFL was theoretically predicted.<sup>[135]</sup> Following two successive studies, the pulse-forming mechanism of dissipative soliton resonance (DSR) which generates a rectangular pulse was investigated based on the cubic-quintic Ginzburg-Landau equation.<sup>[136,137]</sup> By tailoring the parameters of a MLFL cavity, the pulse energy can increase infinitely, while the peak power amplitude is kept at a constant level. A flat-top rectangular temporal profile is a typical feature of MLFL working in the DSR regime.<sup>[5]</sup> The demonstration of the DSR regime was realized in an erbium-doped MLFL to generate pulse energies up to 281.2 nJ,<sup>[138]</sup> about



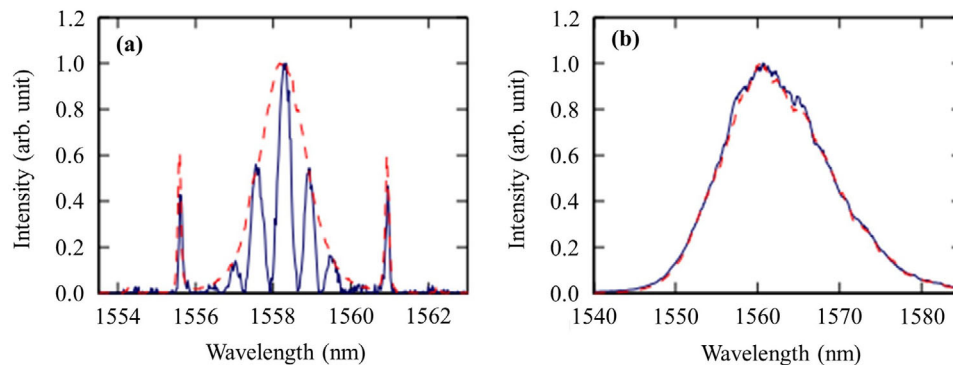


**Figure 15.** a) Spectral interference pattern of consecutive pulses. a) Soliton laser shows phase coherence for DSR regime and b) non-phase coherence for NLP regime. Reproduced with permission.<sup>[145]</sup> Copyright 2013, Optica.

two order-of-magnitude higher than the highest pulse energy generated for MLFL seed source of 4.5 nJ in Table 1.<sup>[72]</sup> In addition, an erbium-ytterbium-doped MLFL using double-clad fiber working in the DSR regime was demonstrated to generate a rectangular pulse with pulse energy up to 2.12<sup>[139]</sup> and 2.27  $\mu\text{J}$ .<sup>[38]</sup> Therefore, the MLFL working in the DSR regime could serve as a reliable source with high-energy rectangular-shape pulses.

Apart from the DSR regime, a MLFL working in the noise-like pulse (NLP) regime could also exhibit a flat-top rectangular pulse. The main difference between DSR and NLP is that the DSR pulse is a single pulse, whereas the NLP is a wave packet composed of numerous sub-picosecond pulses with varying width and peak intensity.<sup>[140]</sup> The NLP demonstrates a pulse packet with a complex internal structure where the pulses exhibit chaotic motion.<sup>[141]</sup> Nevertheless, this pulse packet conserves stable temporal envelope, average amplitude, pulse energy, and the corresponding spectrum as a whole. Observing with a large time scale, the NLP shows analogous behavior to soliton, which shows a train of pulse packets. Therefore, the NLP shows a typical sub-picosecond coherent spike on top of a wide pedestal on an autocorrelation trace. In contrast to solitary pulse, the NLP features an outstanding increase in pulse energy that can reach up to  $\mu\text{J}$  level, but with low coherence and larger pulse width.<sup>[142]</sup>

In certain scenarios, the setting of a particular set of laser cavity parameters can result in a scheme where it is hardly distinguishable between the DSR and the NLP regime.<sup>[54]</sup> This issue has been shown in some works demonstrated in a Fo8 laser cavity<sup>[143]</sup> and a ring cavity.<sup>[144]</sup> There are two experimental techniques to identify a rectangular pulse MLFL whether working in the DSR or the NLP schemes. The first technique is the spectral measurement using an autocorrelator. In contrast to NLP that presents a spike appeared on top of a wide pedestal, the absence of a spike and any fine-structure hidden in the pulse envelope validates the laser works in the DSR regime. The second technique is the implementation of an interference method to determine the phase coherence of a rectangular pulse MLFL according to a phase coherence experiment.<sup>[145]</sup> This setup corresponds to a Michelson interferometer with a path difference of one cavity roundtrip between the arms of the device. Based on the optical spectrum, the laser pulse should exhibit a coherent pulse when operating in the DSR regime as presented in Figure 15a. The solid and dashed curves denote the output of the interferometer and laser output,

respectively. On the other hand, the laser pulse does not exhibit phase correlations among pulses for laser pulse produced in the NLP regime as shown in Figure 15b.

#### 4.1. Dissipative Soliton Resonance

The DSR pulse was obtained in the frame of the cubic-quintic complex Ginzburg-Landau equation, where the pulse width of the MLFL increases in a rectangular profile with increasing pump power without wave breaking or pulse splitting, thus infinitely increasing the pulse energy while simultaneously keeping the peak power at a constant amplitude.<sup>[54,136,146]</sup> This is due to the peak power clamping (PPC) effect that plays an important role in the generation of the DSR pulses.<sup>[147]</sup> The DSR generates nanosecond pulses with a large chirp and large pulse energy directly in a main laser resonator.<sup>[71]</sup> The DSR operation can be obtained in both the anomalous and the normal dispersion regions.<sup>[148,149]</sup> Subsequently, a large value of net cavity dispersion is the fundamental parameter that determines whether the stable high-power DSR mode-locking regime can be achieved while circumventing unwanted MPIs.<sup>[135–137]</sup> Another intrinsic characteristic of the DSR pulses is the amplitude envelope modulation observed through the RF spectrum.<sup>[54,139]</sup> The modulation period is directly connected to the reciprocal of the duration of the generated pulses, which becomes faster with increasing pump power.

A long SMF-28e or highly nonlinear fiber (HNLF) is typically employed to enhance the nonlinear phase shift in the Fo9 laser cavity to generate the DSR pulses.<sup>[64,150]</sup> Despite that the core diameters of the SMF-28e and HNLF are different, these fibers can be connected by fusion splicing with repeated arc discharges. Nevertheless, the energy of the DSR pulses generated from HNLF reaches only dozens of nJ owing to the high nonlinear coefficient and large propagation loss of the HNLF.<sup>[151]</sup> Therefore, SMF-28e is more effective than HNLF in achieving high pulse energy. In addition, the energy of DSR pulses is directly proportional to the length of the laser cavity such that a longer laser cavity has a lower fundamental repetition rate, facilitating the generation of higher energy pulses.<sup>[152]</sup> Following this work, an investigation of the influence of the loop length of the Fo9 laser cavity on pulse width and pulse energy was conducted.<sup>[153]</sup> The pulse width increases when the pump power or loop length

of the Fo9 laser cavity is increased. With a longer loop length, the pulse energy of the DSR laser increases more rapidly at the cost of lower peak power owing to longer pulse width.

Apart from increasing the loop length, the reflectivity ( $R_f$ ) of the mirror loop was also studied according to:<sup>[33,153]</sup>

$$R_f = 2\alpha(1 - \alpha)\{1 + \cos[(1 - 2\alpha) \times \gamma PL]\} \quad (6)$$

where  $\alpha$ ,  $\gamma$ ,  $P$ , and  $L$  are the coupling ratio, nonlinear coefficient, optical power, and mirror loop length, respectively. The  $R_f$  gives the remaining amount of the intra-cavity power, which depends periodically on the  $P$  of the mirror loop, thus it is equivalent to periodic saturable absorption that is favorable for the formation of DSR pulse. Moreover, the saturation power of the periodic saturable absorber was shown to determine the peak power of the DSR mode-locked laser pulses.<sup>[147]</sup> The generation of high-power DSR pulses was demonstrated in a Fo9 laser cavity using double-clad erbium-ytterbium-doped fiber that achieves pulse energy of 2.3  $\mu\text{J}$ .<sup>[54]</sup> Besides seed sources, external amplifiers can be used to increase the power and pulse energy of the DSR pulses.<sup>[151]</sup> For instance, a thulium-doped MLFL which generates DSR pulse through a Fo9 laser cavity was amplified through a 3-stage amplifier system to achieve a pulse energy of 330  $\mu\text{J}$ .<sup>[150]</sup> Besides external amplification, remarkable work was demonstrated for visible-wavelength OVBs using a Fo9 laser cavity working in the DSR regime.<sup>[117]</sup> A mode selective coupler (MSC) was employed for transverse mode selection that converts a portion of the fundamental LP01 mode into a higher-ordered LP11 mode output. In this case, the MSC plays a significant role in phase matching between LP01 mode in the SMF-28e and LP11 mode in the few-mode fiber (FMF), which then realizes the mode conversion to the higher-order mode. The propagation constant between LP01 and LP11 modes was matched by tapering the SMF-28e to a specific diameter, and then the SMF-28e and FMF were wound, stretched, and fused together so that the two cores were close to each other. The incorporation of MSC into a Fo9 laser cavity not only delivers picosecond OVBs with topological charges of  $\text{OAM} \pm 1$ , but also improves the purity of LP11 mode to be as high as 97.2%. This is the only demonstration of Fo9 laser cavity operating in the visible wavelength. The rectangular pulse emission operating in the DSR regime is important, in particular for generating high pulse energy of the MLFL. In a non-PM Fo9 laser cavity, an additional long SMF-28e or HNLF was employed to induce nonlinear phase shift to the laser cavity, which also reduces the pulse repetition rate by operating in a single-pulse ML state, thus increasing the pulse energy.<sup>[54,64,139]</sup> The DSR is a viable option to achieve MLFL seed source with a high pulse energy, which can be amplified through multiple-stage amplification to achieve  $\mu\text{J}$  or even mJ level pulses, in the near future.

## 4.2. Noise-Like Pulse

Apart from the DSR pulse, NLP is another type of rectangular pulse MLFL, which has become attractive in recent years due to its broad applications in the generation of supercontinuum,<sup>[154]</sup> fiber Bragg grating interrogation,<sup>[155]</sup> and optical coherence tomography.<sup>[156]</sup> In contrast to DSR which is a single pulse, the NLP exhibits a wave packet consisting of numerous sub-picosecond pulses with varying widths and peak intensities.<sup>[140]</sup>

Recently, investigations on the NLP have been conducted which showed that the NLP could operate in numerous states, such as multiple NLP with various patterns,<sup>[157]</sup> coexistence of harmonic soliton molecules and NLP,<sup>[158]</sup> and switchable generation of NLP and DSR.<sup>[159]</sup> Besides, a study verified the presence of the low-amplitude, drifting sub-pulses that occur in the NLP.<sup>[141]</sup> Benefitting from their weak visibility, the low-amplitude sub-pulses may be overlooked in the study of NLP, especially when the experiment was conducted without the availability of a high-speed detecting system. The conventional NLP was switched to the NLP with low-amplitude, sub-pulses by slightly adjusting the polarization state without significantly influencing the output characteristics of the laser. The observation of this dynamic was achieved using a real-time oscilloscope with a bandwidth of up to 20 GHz, where the detection ability is limited by a 12.5 GHz photodetector. Therefore, such motion dynamics may extensively occur in NLP regime, which might be overlooked due to difficulties in real-time detection.

Apart from conventional NLP which exhibits rectangular pulses with positive intensity, dark pulse behaviors in an opposite manner in which the rectangular pulse has a negative intensity in the oscilloscope traces.<sup>[75]</sup> The dark pulse can be generated in either normal or anomalous dispersion regimes. There are three types of dark pulses, which include NLSE, domain-wall (DW), and cubic-quintic NLSE pulses. The NLSE dark pulses operate in the normal dispersion laser cavity, which depends on the variation of the refractive index within the optical fiber. The DW dark pulses can be generated in both normal and anomalous dispersion laser cavity due to the interaction of two or more wavelength emissions between two orthogonal incoherently coupled polarization components in birefringent optical fibers. The cubic-quintic NLSE dark pulses were generated in the anomalous dispersion laser cavity owing to the strong third and fifth-ordered nonlinearities in the laser cavity. The demonstration of a dark rectangular NLP was conducted in a Fo9 laser with a net anomalous dispersion.<sup>[52,75]</sup> The pump power threshold of the dark rectangular NLP is observed to be 85 mW, and a more stable dark rectangular NLP was achieved at a pump power of 225 mW. At a higher pump power, the PC orientation was carefully adjusted for the generation of a fifth-harmonic dark rectangular pulse with a repetition rate of 1.616 MHz.

In another work, external amplifiers were employed to boost the power of the NLP seed source. For instance, a single-stage amplifier was implemented to amplify a NLP with the center wavelength at 2102.2 nm.<sup>[160]</sup> The output power increased linearly from  $\approx 0.5$  to 5.8 W with a laser slope efficiency of 56.8% as the pump power of the laser cavity was increased from 0.85 to 10.05 W. At the maximum power, the pulse energy was measured to be 1.52  $\mu\text{J}$ . Another amplifier was incorporated to amplify a NLP seed source with a center wavelength of 1950 nm from the average output power of  $\approx 72$  mW to  $\approx 3$  W after amplification.<sup>[85]</sup> The amplified NLP spectra extend to a longer wavelength region of  $\approx 2460$  nm after amplification owing to the self-phase modulation, soliton formation, and subsequent self-frequency shift. The spectrum broadening after amplification indicates the high peak power of the amplified NLP. The amplified NLP can be used to generate mid-infrared supercontinuum spans from  $\approx 1500$  to 4100 nm at a maximum output power of  $\approx 1.45$  W, by connecting a single-mode fiber to an indium fluoride fiber through fusion

**Table 2.** MLFL seed sources generated with a Fo9 laser cavity.

Regime	$\lambda_c$ [nm]	$\Delta\lambda$ [nm]	$P_{\text{pump}}$ [W]	$\tau$ [ns]	$f$ [MHz]	SNR [dB]	$P_{\text{out}}$ [mW]	$E_p$ [nJ]	$P_p$ [W]	Ref.
DSR	634.36	0.16	0.21 to 0.31	0.085–0.51	5.125	63.4	$\approx 0.25$ –1.3	$\approx 0.05$ –0.26	0.45	[117]
DSR	1310	1.59	0.23–0.31	7.2–13.9	0.217	$\approx 36.1$	$\approx 3$ –42.9	$\approx 145$ –197	$\approx 13$ –15	[64]
DSR	1338	10	0.66–1.04	16.4–48	0.362	60	$\approx 3.2$ –11	$\approx 10$ –30	0.6	[5]
NLP	$\approx 1560$	$\approx 8$	0.225–0.4	80.6–11.8 (DP)	0.323–1.616	58	$\approx 4.2$ –8.8	$\approx 15.0$ –27.2	–	[75]
DSR	1566	3.8	0.4–4.8	$\approx 25$ –445	0.412	74	$\approx 50$ –950	$\approx 200$ –2300	4.87	[54]
NLP	1570.9	7.9	0.1–0.5	$\approx 30$ –130	0.4917	54	$\approx 13$ –45	$\approx 26.44$ –91.52	$\approx 0.7$ –0.9	[164]
DSR	1889	$\approx 17$ –20	0.67–2.57	$\approx 180$ –857	0.2888	65	282	$\approx 100$ –1230	$\approx 0.56$ –1.43	[165]
NLP	1907.67	10.22	0.45–1	–	0.3725	40	$\approx 4$ –36.3	$\approx 10.73$ –97.4	–	[125]
NLP	1957.7	$\approx 34.2$	4.2	$\approx 2.3$	$\approx 0.19$	$\approx 52$	$\approx 72$	$\approx 378.9$	164	[166]
DSR	1959.5	16.5	LD1 = 2.2, LD2 = 0–4.5	144.6	$\approx 0.95$	$\approx 62$	$\approx 100.25$ –677.5	$\approx 105.5$ –713.2	$\approx 4$	[77]
NLP	1970.3	16.5	LD1 = 2.4, LD2 = 0.5–1.8	74.47		$\approx 61.4$	$\approx 100$ –429	$\approx 105.3$ –452	$\approx 3.5$	
DSR	$\approx 1976$	12.3–16.6	3.96–7	12–262	0.3178	$\approx 70$	$\approx 1$ –41.5	$\approx 10$ –130.5	$\approx 0.26$ –0.49	[150]
DSR	$\approx 1985$	18	5.5	$\approx 50$	1.65	57	670	400	$\approx 8$	[71]
DSR	2005.9	$\approx 3.4$	1.83–5.49	1.9–13.73	3.37	58.4	$\approx 110$ –1190	40.35–353.11	26	[153]
NLP	2102.2	10.8–11.2	3.71–4.46	5.4–6.95	3.82	64.4	520–670	$\approx 135$ –175.1	$\approx 25.2$	[160]

$\lambda_c$  = center wavelength,  $\Delta\lambda$  = 3-dB spectral bandwidth,  $P_{\text{pump}}$  = pump power,  $\tau$  = pulse width,  $f$  = fundamental repetition rate, SNR = signal-to-noise ratio,  $P_{\text{out}}$  = output power,  $E_p$  = pulse energy,  $P_p$  = peak power, ref. = references, DSR = dissipative soliton resonance, NLP = noise-like pulse, DP = dark pulse, and LD = laser diode.

splicing. Although NLP exhibits a relatively higher noise and less interference coherency than the DSR,<sup>[145]</sup> its importance should not be overlooked, such as the generation of rectangular pulse and dark soliton. On the other hand, the NLP could be amplified through an external amplifier to achieve higher average output power and pulse energy. In addition, the NLP was demonstrated with the generation of supercontinuum covering the near- and mid-infrared wavelengths, which is very important for applications such as optical coherent tomography, hyperspectral imaging, remote sensing, and mid-infrared spectroscopy.<sup>[161–163]</sup>

### 4.3. Summary

**Table 2** summarizes the experimental results on the rectangular pulses generated through the Fo9 laser cavity operating in DSR and NLP regimes. Several remarks have to be given for **Table 2**. For instance, a DSR rectangular pulse was demonstrated in the visible wavelength region.<sup>[117]</sup> In addition, the rectangular pulse was mostly demonstrated at the wavelength regions of  $\approx 1.55$  and  $\approx 2 \mu\text{m}$ , while the rectangular pulse has not been reported in the  $\approx 1 \mu\text{m}$  region. Two studies demonstrated the DSR rectangular pulse at the wavelength of  $\approx 1.3 \mu\text{m}$  using bismuth-doped phosphosilicate optical fibers.<sup>[5,64]</sup> Dark pulses (DPs) were presented with decreasing pulse width characteristics when a higher pump power was employed.<sup>[75]</sup> Simultaneous DSR and NLP rectangular pulses were observed in a Fo9 laser cavity by increasing the pump power from 0.5 to 4.5 W.<sup>[77]</sup> The highest pulse energy of the rectangular pulse was achieved to be  $\approx 2.3 \mu\text{J}$  using a double-clad erbium-ytterbium-doped fiber in a Fo9 laser cavity.<sup>[54]</sup>

## 5. Challenges and Recommendations

Currently, it remains a formidable challenge to reduce the threshold of self-start MLFL and to increase the pulse energy of ultra-short and rectangular pulse MLFL. For instance, there are still

issues with the self-starting MLFL of a Fo9 laser cavity, which restricts the possibility of achieving even higher output energy. A non-reciprocal phase shifter inserted in a Fo9 laser cavity with an asymmetric NALM leads to an accumulation of  $\Delta\phi_{\text{NL}}$  between counter-propagating beams along the NALM from the power fluctuations of a continuous wave laser. Therefore, the self-starting of MLFL requires that the slope of the SA transmittance curve should be as large as possible.<sup>[35]</sup> In addition, the  $\Delta\phi_{\text{NL}}$  must be located within a certain range of the SA transmission curve to achieve a higher SA transmission for single pulse operation.<sup>[167,168]</sup> However, the nonlinear phase shift between counter-propagating beams was induced due to the asymmetrical NALM which causes the CW and CCW optical fields to exhibit different transmission slopes as a function of pump power. The increase of pump power would easily exceed the value of  $\Delta\phi_{\text{NL}}$  allowed for single pulse operation, which restricts further increase of pulse energy. Moreover, a large asymmetrical NALM structure hampers the manipulation of net cavity dispersion and nonlinearity to increase the pulse energy.<sup>[79]</sup> Under strong pumping, the continuous wave laser power is extremely high. This causes the gain fiber to operate in deep saturation, giving rise to the “self-healing” effect which is a drawback for amplifying weak power fluctuations of continuous wave laser and causes difficulty in achieving self-starting MLFL.<sup>[169]</sup> There are several recommendations to assist the self-starting of MLFL and increase the pulse energy of the Fo9 laser cavity. A material-based SA can be utilized to build a hybrid Fo9 laser cavity to assist the self-start MLFL.<sup>[170]</sup> The combination of two SAs in a laser cavity solves the self-start mode-locking problem with improved pulse quality.<sup>[171]</sup> Furthermore, a photonics crystal fiber that has a polarized large mode area can be utilized to support environmentally stable high-power operation and achieve high-energy laser pulses.<sup>[81]</sup> Moreover, a higher pulse energy can be achieved with a thulium-holmium-doped fiber (THDF) due to its higher pump efficiency than a thulium-doped fiber where the

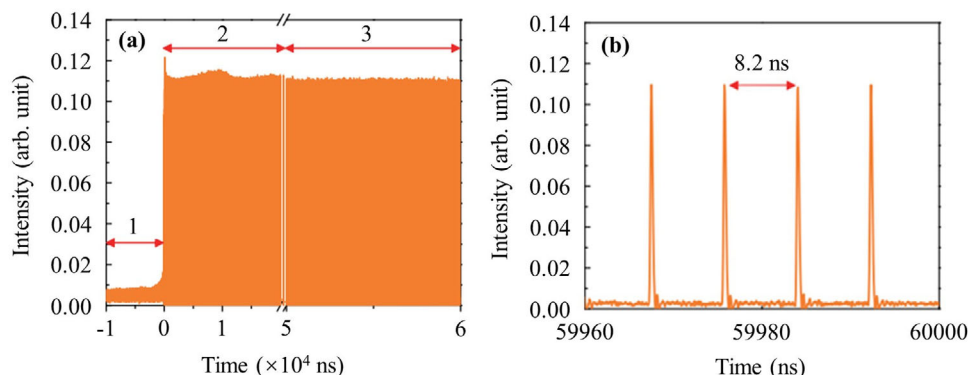


**Figure 16.** a) Build-up process of self-start MLFL with three regions including exponential growth, damping, and steady states. b) A zoom-in observation of the Region 3. Reproduced with permission.<sup>[6]</sup> Copyright 2019, Chinese Physical Society and IOP Publishing Ltd.

absorption efficiency of THDF is improved with a higher absorption efficiency.<sup>[172]</sup>

Apart from optimizing the Fo9 laser cavity parameters to achieve self-start MLFL with higher pulse energy, the real-time investigation of the self-starting dynamics process remains at an infancy stage. The dynamics of MLFL could be studied with a time-stretched dispersive Fourier transform (TS-DFT) method.<sup>[58,59]</sup> The fast response time of the photodetection in the TS-DFT system makes it possible to reveal the shot-to-shot spectral information over consecutive roundtrips at a scan rate that is measurable by a high-speed oscilloscope. The TS-DFT technique is expected to improve the dynamics study of the buildup process of self-starting MLFL in a Fo9 laser cavity which was recorded with three regions in Figure 16a.<sup>[6]</sup> An exponential growth was observed at the first region due to fast non-saturable extraction of the stored energy in the active fiber. After reaching the peak, a slight damping process of pulse amplitudes occurs which lasts for  $\approx 40$   $\mu$ s, prior to the formation of the stable mode-locking state. Region 3 was enlarged in Figure 16b, which shows a pulse interval of 8.2 ns, corresponding to the cavity round-trip time for a single pulse operation with the fundamental pulse repetition rate. The TS-DFT technique has been employed to study the period multiplication, such as periodic quadrupling between fundamental mode-locking operation and pulse splitting states of a Fo9 laser cavity.<sup>[173]</sup> A main difference between these two states is that a uniform pulse intensity was observed in the former regime. For period quadrupling, the pulse intensity has strong spectral intensity modulation which alters between four different values, denoted by the switching of a steady-state period from 1 to 4 roundtrip times. The pulse spacing of the period quadrupling state remains at a constant of 36.5 ns, where the intensity modulation would generate new frequency comb lines in the RF spectrum. According to the theory of Fourier transform, a strong intensity modulation will result in frequency comb lines with a high energy and vice versa. Apart from periodic bifurcation, several other interesting phenomena of self-start MLFL were recently reviewed, which is expected to bring a comprehensive understanding of how TS-DFT technique can be used to understand the dynamics of self-start MLFL.<sup>[80,174]</sup> These studies will enrich insight into self-start MLFL through a Fo9 laser cavity, which could be an interesting direction in the future.

There are numerous factors affecting the MLFL generated based on the Fo9 laser cavity. For instance, the manipulation of polarization states by waveplate settings affects the self-start MLFL operation<sup>[49]</sup> and wavelength tunability.<sup>[69]</sup> Therefore, the investigation of precise polarization angle variation for the MLFL operation is recommended, such as the utilizing of a polarimeter system together with PBS or a polarization controller with displayed angles.<sup>[175]</sup> Different polarization angle leads to wavelength tunability since the  $\Delta\phi_{NL}$  has a direct influence on the wavelength.<sup>[89]</sup> Apart from the waveplate settings, some researchers studied the difference between output and reject ports of the Fo9 laser cavity in terms of 3-dB spectral bandwidth, pulse duration, pulse energy, RIN, etc. In particular, the output port has typically lower RIN value, whereas the rejected port tends to have a more complicated optical spectrum and spectral phase.<sup>[105,176]</sup> Apart from the above parameters, the fundamental pulse repetition rate is difficult to measure owing to the generation of self-start multiple pulses at high pump powers.<sup>[62]</sup> The use of the pump hysteresis method by decreasing the initial high pump power to obtain a single pulse is a problem that needs to be overcome for the Fo9 laser cavity. In the Fo9 laser cavity, the use of a phase shifter is important to induce non-reciprocal phase bias, which may be inserted in either a transmissive or reflective manner. A transmissive-type phase shifter (TPS) was incorporated typically inside the NALM. On the other hand, a reflective-type phase shifter (RPS) was employed typically in the mirror loop arm that reduces the laser cavity complexity. For instance, the RPS was constructed from a Wollaston prism, a FR, a  $\lambda/8$  WP, and a mirror.<sup>[47,177]</sup> The RPS was incorporated to compare the self-start MLFL threshold and phase noise with the optimized performance obtained by using  $\lambda/8$  WP, as compared to  $\lambda/6$  and  $\lambda/10$  waveplates.<sup>[50]</sup> From a commercialization perspective, the RPS was demonstrated with the operating wavelengths of  $\approx 1.03$ , 1.56, and 2.05  $\mu$ m by Menlo Systems GmbH under the trademark figure9<sup>TM</sup>. To date, there exists a research gap for comparison between the TPS and RPS. Hence, understanding how TPS and RPS affect the MLFL performance could be an important direction for experimental research which could help to further optimize the Fo9 laser cavity structure in the future.

According to Table 1, the picosecond and femtosecond MLFL seed sources based on a Fo9 laser cavity are most working on  $\approx 1.06$  and  $\approx 1.55$   $\mu$ m regions. Such MLFL working between  $\approx 1.7$



and 2.1  $\mu\text{m}$  are rare, thus suggesting the potential technological importance of future research. According to Table 2, the DSR and NLP play an equally important role in generating rectangular pulse MLFL. Surprisingly, rectangular pulse MLFL has not been reported in the popular  $\approx 1.06$   $\mu\text{m}$  region, although some unique wavelengths, such as  $\approx 0.63$  and  $\approx 1.31$   $\mu\text{m}$ , have been reported. The investigation of the reason that limits the generation of rectangular pulse ytterbium-doped MLFL therefore could be of much interest. In addition, the mechanism of forming bright and dark rectangular pulse through a Fo9 laser cavity should be studied, especially dark pulse is more stable in noise circumstances, less susceptible to loss, and broadened during propagation at nearly half the rate of bright solitons.<sup>[178,179]</sup> In both Tables 1 and 2, the near-infrared wavelengths regions between  $\approx 1.06$  and  $\approx 1.55$   $\mu\text{m}$ , and  $\approx 1.55$  to 1.7  $\mu\text{m}$  are obvious gaps that cannot be easily fulfilled by rare-earth doped laser gain medium. However, these gaps might be fulfilled by using the bismuth-doped fiber laser.<sup>[180]</sup> In addition, the Fo9 laser cavity is expected to be exploited further in the visible and mid-infrared wavelength regions in the future, following some recent works on MLFL lasers operating in these wavelength regions.<sup>[181,182]</sup>

## 6. Conclusion and Outlook

We have presented a comprehensive discussion on Fo9 laser cavity, with a focus on the comparison with other artificial SAs, pulse formation mechanisms, cavity optimization, and experimental setup. The Fo9 laser cavity has been implemented to generate picosecond and femtosecond MLFL through the manipulation of experimental parameters, such as net cavity dispersion, polarization state, and pump hysteresis. The optical measurement at the output and reject ports enables an interesting pulse performance analysis on the wavelength tunability, repetition rate, noise suppression, and OVBs. The Fo9 laser cavity has also been employed for the generation of rectangular pulse MLFL through the DSR and NLP regimes. The combination of rectangular pulse emission with the Fo9 laser cavity facilitates the generation of a higher pulse energy as a higher optical power is fully recycled, measured, and utilized at another exit port of the coupler in comparison to the Fo8 laser cavity. The pulse energy could be over two-order of magnitude higher than the highest pulse energy generated by the ultrafast MLFL seed source through the Fo9 laser cavity. The current issues and challenges of laser pulse formation in the Fo9 laser cavity were discussed and some recommendations for future research directions were highlighted. This review is expected to provide insight into the pulse formation mechanism and optimization methods based on the Fo9 laser cavity, which is anticipated to become the next generation of artificial SA with interesting laser features and output performances that could be of growing interest to the laser community.

## Acknowledgements

This work was financially supported by the National Key R&D Program of China (Nos. 2020YFB1805900 and 2021YFB2802000) and the National Natural Science Foundation of China (Grant No. U20A20211). The authors also thank the financial support from the National Natural Science Foundation of China (Grant Nos. 62175210, 62005240 and W2433154) and the Natural Science Foundation of Zhejiang Province (Grant Nos. LY21F050005 and LR21E020005).

## Conflict of Interest

The authors declare no conflict of interest.

## Keywords

artificial saturable absorber, figure-of-nine laser cavity, mode-locked fiber laser, rectangular pulse emission

Received: November 26, 2023

Revised: August 20, 2024

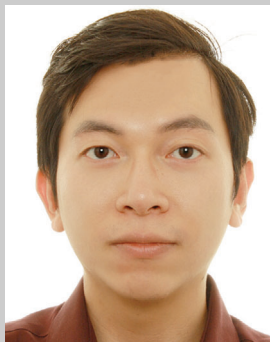
Published online:

- [1] D. Duan, J. Wang, Y. Wu, J. Ma, Q. Mao, *Opt. Express* **2020**, *28*, 33603.
- [2] U. Keller, *Nature* **2003**, *424*, 831.
- [3] S. R. Hutter, A. Seer, T. König, R. Herda, D. Hertzsch, H. Kempf, R. Wilk, A. Leitenstorfer, *Laser Photon. Rev.* **2023**, *17*, 2200907.
- [4] Z. Łaszczych, G. Soboń, *Opt. Express* **2021**, *29*, 2690.
- [5] H. Ahmad, S. N. Aidit, S. I. Ooi, M. Z. Samion, S. Wang, Y. Wang, J. K. Sahu, A. K. Zamzuri, *Sci. Rep.* **2021**, *11*, 6356.
- [6] K. Yin, Y.-M. Li, Y.-B. Wang, X. Zheng, T. Jiang, *Chinese Phys. B* **2019**, *28*, 124203.
- [7] L. A. Gomes, L. Orsila, T. Jouhti, O. G. Okhotnikov, *IEEE J. Sel. Top. Quantum Electron.* **2004**, *10*, 129.
- [8] K. Kieu, F. W. Wise, *Opt. Express* **2008**, *16*, 11453.
- [9] K. Y. Lau, X. Liu, J. Qiu, *Adv. Photonics Res.* **2022**, *3*, 2200023.
- [10] U. Keller, D. A. B. Miller, G. D. Boyd, T. H. Chiu, J. F. Ferguson, M. T. Asom, *Opt. Lett.* **1992**, *17*, 505.
- [11] U. Keller, K. J. Weingarten, F. X. Kärtner, D. Kopf, B. Braun, I. D. Jung, R. Fluck, C. Hönninger, N. Matuschek, J. A. D. Au, *IEEE J. Sel. Top. Quantum Electron.* **1996**, *2*, 435.
- [12] K. Viskontas, K. Regelskis, N. Rusteika, *Lith. J. Phys.* **2014**, *54*, 127.
- [13] S. Y. Set, H. Yaguchi, Y. Tanaka, M. Jablonski, Y. Sakakibara, A. Rozhin, M. Tokumoto, H. Kataura, Y. Achiba, K. Kikuchi, in *OFC 2003 Optical Fiber Communications Conf.*, 2003 Atlanta, Georgia, United States March **2003**.
- [14] Q. Bao, H. Zhang, Y. Wang, Z. Ni, Y. Yan, Z. X. Shen, K. P. Loh, D. Y. Tang, *Adv. Funct. Mater.* **2009**, *19*, 3077.
- [15] X. Liu, D. Popa, N. Akhmediev, *Phys. Rev. Lett.* **2019**, *123*, 093901.
- [16] Y. Yang, L. Zhong, Y. Cui, Y. Wang, D. Chen, K. Y. Lau, X. Liu, Z. Ma, G. Barillaro, Z. Chen, J. Qiu, *Nanophotonics* **2023**, *12*, 3069.
- [17] X. Liu, Y. Cui, *Adv. Photonics* **2019**, *1*, 1.
- [18] K. Y. Lau, D. Hou, *Opt. Laser Technol.* **2021**, *137*, 106826.
- [19] D. C. Kirsch, S. Chen, R. Sidharthan, Y. Chen, S. Yoo, M. Chernysheva, *J. Appl. Phys.* **2020**, *128*, 180906.
- [20] S. Y. Ryu, K.-S. Kim, J. Kim, S. Kim, *Opt. Express* **2012**, *20*, 12966.
- [21] P. V. Mamyshev, in *24th European Conference on Optical Communication (ECOC)*, **1998**, *1*, 475.
- [22] Z. Liu, Z. M. Ziegler, L. G. Wright, F. W. Wise, *Optica* **2017**, *4*, 649.
- [23] E. P. Ippen, H. A. Haus, L. Y. Liu, *J. Opt. Soc. Am. B* **1989**, *6*, 1736.
- [24] S. M. Koltsev, *Opt. Fiber Technol.* **2022**, *68*, 102764.
- [25] H. A. Haus, E. P. Ippen, K. Tamura, *IEEE J. Quantum Electron.* **1994**, *30*, 200.
- [26] S. Wang, C. R. Menyuk, S. Droste, L. Sinclair, I. Coddington, N. Newbury, *Opt. Lett.* **2017**, *42*, 2362.
- [27] M. Hofer, M. E. Fermann, F. Haberl, M. H. Ober, A. J. Schmidt, *Opt. Lett.* **1991**, *16*, 502.
- [28] N. Nishizawa, H. Suga, M. Yamanaka, *Opt. Express* **2019**, *27*, 19218.
- [29] N. Kuse, J. Jiang, C. C. Lee, T. R. Schibli, M. E. Fermann, *Opt. Express* **2016**, *24*, 3095.
- [30] Y. Feng, X. Xu, X. Hu, Y. Liu, Y. Wang, W. Zhang, Z. Yang, L. Duan, W. Zhao, Z. Cheng, *Opt. Express* **2015**, *23*, 17549.

- [31] M. E. Fermann, M. L. Stock, M. J. Andrejco, Y. Silberberg, *Opt. Lett.* **1993**, 18, 894.
- [32] J. Szczepanek, T. M. Kardas, C. Radzewicz, Y. Stepanenko, *Opt. Lett.* **2017**, 42, 575.
- [33] N. J. Doran, D. Wood, *Opt. Lett.* **1988**, 13, 56.
- [34] M. E. Fermann, F. Haberl, M. Hofer, H. Hochreiter, *Opt. Lett.* **1990**, 15, 752.
- [35] W. Hänsel, H. Hoogland, M. Giunta, S. Schmid, T. Steinmetz, R. Doubek, P. Mayer, S. Dobner, C. Cleff, M. Fischer, R. Holzwarth, *Appl. Phys. B* **2017**, 123, 41.
- [36] C. Aguerararay, R. Hawker, A. F. J. Runge, M. Erkintalo, N. G. R. Broderick, *Appl. Phys. Lett.* **2013**, 103, 121111.
- [37] J. Szczepanek, T. M. Lardas, M. Michalska, C. Radzewicz, Y. Stepanenko, *Opt. Lett.* **2015**, 40, 3500.
- [38] G. Semaan, F. B. Braham, M. Salhi, Y. Meng, F. Bahloul, F. Sanchez, *Opt. Express* **2016**, 24, 8399.
- [39] F. O. Ilday, F. W. Wise, *Opt. Lett.* **2002**, 27, 1531.
- [40] J. W. Nicholson, M. Andrejco, *Opt. Express* **2006**, 14, 8160.
- [41] Y. Shirakura, K. Takiguchi, S. Y. Set, S. Yamashita, in Conference on Laser and Electro-Optics CLEO, Optica Publishing Group, San Jose, CA, USA **2018**.
- [42] T. F. Carruthers, I. N. Duling, M. L. Dennis, *Electron. Lett.* **1994**, 30, 1051.
- [43] D. J. Jones, L. E. Nelson, H. A. Haus, E. P. Ippen, *IEEE J. Sel. Top. Quant. Electron.* **1997**, 3, 1076.
- [44] K. Tamura, J. Jacobson, E. P. Ippen, H. A. Haus, J. G. Fujitomo, *Opt. Lett.* **1993**, 18, 220.
- [45] H. A. Haus, I. P. Ippen, *Opt. Lett.* **1991**, 16, 1331.
- [46] R. Liao, Y. Song, L. Chai, M. Hu, *Opt. Express* **2019**, 27, 14705.
- [47] T. Jiang, Y. Cui, P. Lu, C. Li, A. Wang, Z. Zhang, *IEEE Photonics Technol. Lett.* **2016**, 28, 1786.
- [48] D. Duan, Q. Lu, B. Wu, Y. Mao, Z. Zhang, J. Ma, B. Yao, S. Wei, Q. Mao, *Opt. Express* **2021**, 29, 23967.
- [49] Z. Łaszczysz, M. Krakowski, G. Soboń, *Appl. Sci.* **2022**, 12, 10613.
- [50] X. Liu, G. Liu, R. Zhou, D. Yu, J. Wu, H. Y. Fu, Z. Zhang, Q. Li, *Laser Phys* **2020**, 30, 085104.
- [51] S. Smirnov, S. Kobtsev, A. Ivanenko, A. Kokhanovskiy, A. Kemmer, M. Gervaziev, *Opt. Lett.* **2017**, 42, 1732.
- [52] R. Zhou, X. Liu, D. Yu, Q. Li, H. Y. Fu, in Asia Communications and Photonics Conference (ACPC) 2019, OSA Technical Digest (Optica Publishing Group), Chengdu, China **2019**.
- [53] T. Asai, H. Yoshimi, J. Shou, T. Fujita, Y. Ozeki, in Conference on Laser and Electro-Optics CLEO, Optica Publishing Group, San Jose, CA, USA **2018**.
- [54] K. Krzempek, J. Sotor, K. Abramski, *Opt. Lett.* **2016**, 41, 4995.
- [55] Y. Ma, B. Xu, H. Ishii, F. Meng, Y. Nakajima, I. Matsushima, T. R. Schibli, Z. Zhang, K. Minoshima, *Opt. Lett.* **2018**, 43, 4136.
- [56] M. Lezius, T. Wilken, C. Deutsch, M. Giunta, O. Mandel, A. Thaller, V. Schkolnik, M. Schiemangk, A. Dinkelaker, A. Kohfeldt, A. Wicht, M. Krutzik, A. Peters, O. Hellmig, H. Duncker, K. Sengstock, P. Windpassinger, K. Lampmann, T. Hülsing, W. Hänsch, R. Holzwarth, *Optica* **2016**, 3, 1381.
- [57] T. Jannson, *Opt. Lett.* **1983**, 8, 232.
- [58] G. Herink, B. Jalali, C. Ropers, D. R. Solli, *Nat. Photon.* **2016**, 10, 321.
- [59] G. Herink, F. Kurtz, B. Jalali, D. R. Solli, C. Ropers, *Science* **2017**, 356, 50.
- [60] K. Y. Lau, Y. Cui, X. Liu, J. Qiu, *Laser Photon. Rev.* **2023**, 17, 2200763.
- [61] K. Y. Lau, S. Firstov, Z. Luo, M. Hu, A. Senatorov, A. Umnikov, B. Xu, X. Liu, J. Qiu, *J. Light. Technol.* **2024**, 42, 2103.
- [62] Z.-W. Lin, J.-X. Chen, T.-J. Li, Z.-Y. Zhan, M. Liu, C. Li, A.-P. Luo, P. Zhou, W.-C. Xu, Z.-C. Luo, *Opt. Express* **2022**, 30, 32347.
- [63] W.-B. Chen, T.-J. Li, L.-Y. Tong, K. Yang, M. Liu, A.-P. Luo, Z.-R. Zhang, Z.-C. Luo, W.-C. Xu, *Opt. Express* **2023**, 31, 2902.
- [64] K. Y. Lau, S. Firstov, Y. Cui, X. Liu, F. Afanasiev, J. Qiu, *J. Light. Technol.* **2023**, 41, 6383.
- [65] E. Baumann, F. R. Giorgetta, J. W. Nicholson, W. C. Swann, I. Coddington, N. R. Newbury, *Opt. Lett.* **2009**, 34, 638.
- [66] H. Lin, D. K. Donald, W. V. Sorin, *J. Light. Technol.* **1994**, 12, 1121.
- [67] H. Yoshimi, K. Sumimura, Y. Ozeki, *Jpn. J. Appl. Phys.* **2018**, 57, 108001.
- [68] K. Y. Lau, A. Pyymaki Perros, D. Li, M. Kim, Z. Sun, *Nanoscale* **2021**, 13, 9873.
- [69] H. Zhang, H. Xia, M. Fan, J. Zheng, J. Li, X. Tian, D. Zhou, Z. Huang, F. Zhang, R. Zhang, Z. Peng, Q. Zhu, *Photonics* **2023**, 10, 184.
- [70] Y. Ma, S. H. Salman, C. Li, C. Mahnke, Y. Hua, S. Droste, J. Fellingner, A. S. Mayer, O. H. Heckl, C. M. Heyl, I. Hartl, *J. Light. Technol.* **2021**, 39, 4431.
- [71] S. Kharitonov, C. S. Brès, presented at *The European Conference on Lasers and Electro-Optics*, Munich, Germany, June **2017**.
- [72] K. Guo, C. Li, B. Ren, T. Wang, J. Wu, Z. Luo, P. Zhou, Z. Jiang, *Opt. Express* **2022**, 30, 35636.
- [73] J. Zhou, W. Pan, X. Fu, L. Zhang, Y. Feng, *Opt. Fiber Technol.* **2019**, 52, 101963.
- [74] Y. Shi, Z. Peng, Z. Cheng, T. Xia, H. Zhao, S. Wan, P. Wang, *IEEE Photonics Technol. Lett.* **2022**, 34, 251.
- [75] R. Zhou, D. Yu, X. Liu, Q. Li, H. Y. Fu, *Opt. Lett.* **2019**, 44, 3717.
- [76] X. Zhang, C. Gu, G. Chen, B. Sun, L. Xu, A. Wang, H. Ming, *Opt. Lett.* **2012**, 37, 1334.
- [77] K. Zhao, P. Wang, Y. Ding, S. Yao, L. Gui, X. Xiao, C. Yang, *Appl. Phys. Express* **2019**, 12, 012002.
- [78] A. Khagai, M. Melkomov, K. Riumkin, V. Khopin, S. Firstov, E. Dianov, *Opt. Lett.* **2018**, 43, 1127.
- [79] F. W. Wise, A. Chong, W. H. Renninger, *Laser Photonics Rev.* **2008**, 2, 58.
- [80] K. Y. Lau, Y. Cui, X. Liu, J. Qiu, *Laser Photon. Rev.* **2023**, 2100763, 1.
- [81] H. Chu, S. Zhao, G. Li, M. Li, D. Li, *Opt. Commun.* **2021**, 482, 126595.
- [82] W. Liu, H. Shi, J. Cui, C. Xie, Y. Song, C. Wang, M. Hu, *Opt. Lett.* **2018**, 43, 2848.
- [83] S. Yuan, L. Si, J. Chen, J. Chen, H. Yu, *Materials* **2022**, 15, 7038.
- [84] Z. Łaszczysz, G. Soboń, *Opt. Laser Technol.* **2022**, 152, 108107.
- [85] B. Ren, C. Li, T. Wang, K. Guo, P. Zhou, *J. Light. Technol.* **2023**, 41, 733.
- [86] J. Li, W. Jiang, Y. Meng, F. Wang, *Opt. Lett.* **2022**, 47, 2606.
- [87] J. Li, W. Jiang, Y. Meng, F. Wang, *Opt. Lett.* **2022**, 47, 5668.
- [88] S. Namiki, E. P. Ippen, H. A. Haus, C. X. Yu, *J. Opt. Soc. Am. B* **1997**, 14, 2099.
- [89] A. S. Mayer, W. Grosinger, K. Fellingner, G. Winkler, L. W. Perner, S. Droste, S. H. Salman, C. Li, C. M. Heyl, I. Hartl, O. H. Heckl, *Opt. Express* **2020**, 28, 18946.
- [90] R. I. Woodward, E. J. R. Kelleher, *Sci. Rep.* **2016**, 6, 37616.
- [91] G. Pu, L. Yi, L. Zhang, W. Hu, *Optica* **2019**, 6, 362.
- [92] J. Zhou, W. Qi, W. Pan, Y. Feng, *Opt. Lett.* **2020**, 45, 5768.
- [93] D. Deng, H. Zhang, Q. Gong, L. He, D. Li, M. Gong, *Opt. Laser Technol.* **2020**, 125, 106010.
- [94] T. Fujita, Y. Ozeki, presented at Conference on Laser and Electro-Optics CLEO, Optica Publishing Group, San Jose, CA, USA **2017**.
- [95] Y. Ozeki, T. Fukazu, presented at Conference on Laser and Electro-Optics CLEO, Optica Publishing Group, San Jose, CA, USA **2016**.
- [96] G. Gao, S. Wang, Z. Zhao, Q. Zhao, Z. Cong, Z. Liu, *Opt. Lett.* **2022**, 47, 5869.
- [97] C. Kerse, H. Kalaycıoğlu, P. Elahi, B. Çetin, D. K. Kesim, Ö. Akçaalan, S. Yavaş, M. D. Aşık, B. Öktem, H. Hoogland, R. Holzwarth, F. Ö. Ilday, *Nature* **2016**, 538, 84.
- [98] T. Udem, J. Reichert, R. Holzwarth, T. W. Hänsch, *Phys. Rev. Lett.* **1999**, 82, 3568.
- [99] Q. Deng, K. Yin, J. Zhang, X. Zheng, T. Jiang, *IEEE Photonics J* **2021**, 13, 1500605.

- [100] W. Gao, G. Liu, Z. Zhang, *Chinese Opt. Lett.* **2018**, 16, 111401.
- [101] G. Liu, X. Jiang, B. Wang, T. Jiang, A. Wang, Z. Zhang, *Laser Phys. Lett.* **2017**, 14, 085103.
- [102] G. Liu, A. Wang, Z. Zhang, *IEEE Photonics Technol. Lett.* **2017**, 29, 2055.
- [103] G. Liu, X. Jiang, A. Wang, G. Chang, F. Kaertner, Z. Zhang, *Opt. Express* **2018**, 26, 26003.
- [104] P. Yan, H. Hu, Z. Li, W. Xu, *Opt. Commun.* **2022**, 513, 128081.
- [105] M. Edelmann, Y. Hua, K. Şafak, F. X. Kärtner, *Opt. Lett.* **2021**, 46, 1752.
- [106] H. Cheng, Z. Zhang, R. Pan, T. Zhang, Y. Feng, X. Hu, Y. Wang, S. Wu, *Opt. Laser Technol.* **2023**, 158, 108818.
- [107] J. Kim, Y. Song, *Adv. Opt. Photon.* **2016**, 8, 465.
- [108] M. E. Fermann, I. Hartl, *Nat. Photon.* **2013**, 7, 868.
- [109] I. Coddington, N. Newbury, W. Swann, *Optica* **2016**, 3, 414.
- [110] H. Timmers, A. Kowligy, A. Lind, F. C. Cruz, N. Nander, M. Silfies, G. Ycas, T. K. Allison, P. G. Schunemann, S. B. Papp, S. A. Diddams, *Optica* **2018**, 5, 727.
- [111] D. J. Jones, S. A. Diddams, J. K. Ranka, A. Stentz, R. S. Windeler, J. L. Hall, S. T. Cundiff, *Science* **2000**, 288, 635.
- [112] Y. Li, N. Kuse, A. Rolland, Y. Stepanenko, C. Radzewicz, M. E. Fermann, *Opt. Express* **2017**, 25, 18017.
- [113] N. Kuse, C.-C. Lee, J. Jiang, C. Mohr, T. R. Schibli, M. E. Fermann, *Opt. Express* **2015**, 23, 24342.
- [114] T. R. Schibli, J. Kim, O. Kuzucu, J. T. Gopinath, S. N. Tandon, G. S. Petrich, L. A. Kolodziejski, J. G. Fujimoto, E. P. Ippen, F. X. Kaertner, *Opt. Lett.* **2003**, 28, 947.
- [115] M. Zhao, R. Yang, X. Jin, Z. Chen, A. Wang, Z. Zhang, Q. Li, *J. Light. Technol.* **2024**, 42, 1651.
- [116] Q. Zhan, *Adv. Opt. Photonics* **2009**, 1, 1.
- [117] H. Sun, L. Wang, J. Zou, Q. Ruan, Y. Ding, C. Dong, Z. Dong, Z. Luo, *J. Light. Technol.* **2022**, 40, 191.
- [118] J. Zou, H. Wang, W. Li, T. Du, B. Xu, N. Chen, Z. Cai, Z. Luo, *IEEE Photonics Technol. Lett.* **2019**, 31, 1487.
- [119] J. Feng, J. Zhou, J. Xu, Y. Feng, X. Zeng, *IEEE Photonics Technol. Lett.* **2022**, 34, 625.
- [120] D. Mao, M. Li, Z. He, X. Cui, H. Lu, W. Zhang, H. Zhang, J. Zhao, *APL Photon* **2019**, 4, 060801.
- [121] T. Wang, F. Wang, F. Shi, F. Pang, S. Huang, T. Wang, S. Zeng, *J. Light Technol.* **2017**, 35, 2161.
- [122] Y. Duan, J. Zhou, L. Wang, Y. Huang, Y. Li, Y. Feng, *Opt. Fiber Technol.* **2021**, 64, 102550.
- [123] L. Liang, Y. Wang, Q. Hu, K. Ren, Y. Zheng, L. Zhu, L. Li, D. Han, *Infrared Phys. Technol.* **2023**, 131, 104688.
- [124] S. Xiong, D. Luo, Y. Liu, W. Wang, Z. Deng, Z. Tang, G. Xie, L. Zhou, Z. Zuo, C. Gu, W. Li, *Opt. Express* **2023**, 31, 514.
- [125] X. Wang, Q. Xia, B. Gu, *Opt. Commun.* **2019**, 434, 180.
- [126] D. Anderson, M. Desaix, M. Lisak, M. L. Quiroga-Teixeiro, *J. Opt. Soc. Am. B* **1998**, 9, 1358.
- [127] S. S. Huang, Y. G. Wang, P. G. Yan, G. L. Zhang, J. Q. Zhao, H. Q. Li, R. Y. Lin, *Laser Phys. Lett.* **2014**, 11, 025102.
- [128] J. P. Lauterio-Cruz, J. C. Hernandez-Garcia, O. Pottiez, J. M. Estudillo-Ayala, E. A. Kuzin, R. Rojas-Laguna, H. Santiago-Hernandez, D. Jauregui-Vazquez, *Opt. Express* **2016**, 24, 13778.
- [129] P. Grelu, N. Akhmediev, *Nat. Photonics* **2012**, 6, 84.
- [130] A. Klenke, S. Breitkopf, M. Kienel, T. Gottschall, T. Eidam, S. Hädrich, J. Rothhardt, J. Limpert, A. Tünnermann, *Opt. Lett.* **2013**, 38, 2283.
- [131] G. Sobon, J. Sotor, I. Pasternak, W. Strupinski, K. Krzempek, P. Kaczmarek, K. M. Abramski, *Laser Phys. Lett.* **2013**, 10, 035104.
- [132] A. M. Kaplan, G. P. Agrawal, D. N. Maywar, *IEEE Photonics Technol. Lett.* **2010**, 22, 489.
- [133] K. Ozgoren, B. Oktom, S. Yilmaz, F. O. Ilday, K. Eken, *Opt. Express* **2007**, 19, 17647.
- [134] G. A. Cranch, G. M. H. Flockhart, C. K. Kirkendall, *J. Light. Technol.* **2005**, 23, 3798.
- [135] N. Akhmediev, J. M. Soto-Crespo, P. Grelu, *Phys. Lett. A* **2008**, 372, 3124.
- [136] W. Chang, A. Ankiewicz, J. M. Soto-Crespo, N. Akhmediev, *Phys. Rev. A* **2008**, 78, 023830.
- [137] P. Grelu, W. Chang, A. Ankiewicz, J. M. Soto-Crespo, N. Akhmediev, *J. Opt. Soc. Am. B* **2010**, 27, 2336.
- [138] X. Wu, D. Y. Tang, H. Zhang, L. M. Zhao, *Opt. Express* **2009**, 17, 5580.
- [139] K. Krzempek, *Opt. Express* **2015**, 23, 30651.
- [140] M. Horowitz, Y. Barad, Y. Silberberg, *Opt. Lett.* **1997**, 22, 799.
- [141] J. Wang, J. He, C. Liao, Y. Wang, *Opt. Express* **2019**, 27, 29606.
- [142] X. Zhou, Z. Cheng, Y. Shi, H. Guo, P. Wang, *IEEE Photonics Technol. Lett.* **2018**, 30, 985.
- [143] X.-W. Zheng, Z.-C. Luo, H. Liu, N. Zhao, Q.-Y. Ning, M. Liu, X.-H. Feng, X.-B. Xing, A.-P. Luo, W.-C. Xu, *Appl. Phys. Express* **2014**, 7, 042701.
- [144] J. Liu, Y. Chen, P. Tang, C. Xu, C. Zhao, H. Zhang, S. Wen, *Opt. Express* **2015**, 23, 6418.
- [145] A. F. J. Runge, C. Aguerarar, N. G. R. Broderick, M. Erkintalo, *Opt. Lett.* **2013**, 38, 4327.
- [146] W. Du, H. Li, J. Li, P. Wang, S. Zhang, Y. Liu, *Opt. Express* **2018**, 26, 21314.
- [147] D. Li, D. Tang, L. Zhao, D. Shen, *J. Light. Technol.* **2015**, 33, 3781.
- [148] W. Chang, A. Ankiewicz, J. M. Soto-Crespo, N. Akhmediev, *J. Opt. Soc. Am. B* **2008**, 25, 1972.
- [149] W. Chang, J. M. Soto-Crespo, A. Ankiewicz, N. Akhmediev, *Phys. Rev. A* **2009**, 79, 033840.
- [150] Z. Zheng, D. Ouyang, X. Ren, J. Wang, J. Pei, S. Ruan, *Photonics Res* **2019**, 7, 513.
- [151] J. Zhao, D. Ouyang, Z. Zheng, M. Liu, X. Ren, C. Li, S. Ruan, W. Xie, *Opt. Express* **2016**, 24, 12072.
- [152] K. Krzempek, K. Abramski, *Opt. Express* **2016**, 24, 22379.
- [153] T. Du, W. Li, Q. Ruan, K. Wang, N. Chen, Z. Luo, *Appl. Phys. Express* **2018**, 11, 052701.
- [154] A. Zaytsev, C.-H. Lin, Y.-J. You, C.-C. Chung, C.-L. Wang, C.-L. Pan, *Opt. Express* **2013**, 21, 16056.
- [155] M. A. Putnam, M. L. Dennis, I. N. Duling, C. G. Askins, E. J. Friebele, *Opt. Lett.* **1998**, 23, 138.
- [156] Y. J. You, C. Wang, Y. L. Lin, A. Zaytsev, P. Xue, C. L. Pan, *Laser Phys. Lett.* **2016**, 13, 025101.
- [157] Y.-Q. Huang, Y.-L. Qi, Z.-C. Luo, A.-P. Luo, W.-C. Xu, *Opt. Express* **2016**, 24, 7356.
- [158] Y.-Q. Huang, Z.-A. Hu, H. Cui, Z.-C. Luo, A.-P. Luo, W.-C. Xu, *Opt. Lett.* **2016**, 41, 4056.
- [159] H. Xu, S. P. Chen, Y. Tao, Z. F. Jiang, *IEEE Photonics J* **2019**, 11, 4517.
- [160] D. Zhao, B. Zhang, X. Zhu, S. Liu, L. Yang, J. Hou, *Opt. Express* **2022**, 30, 3601.
- [161] N. M. Isrealson, C. R. Petersen, A. Barh, D. Jain, M. Jensen, G. Hanneschläger, P. T. Lichtenberg, C. Pedersen, A. Podoleanu, O. Bang, *Light Sci. Appl.* **2019**, 8, 1.
- [162] C. R. Petersen, N. Prtljaga, M. Farries, J. Ward, B. Napier, G. R. Lloyd, J. Nallala, N. Stone, O. Bang, *Opt. Lett.* **2018**, 43, 999.
- [163] I. Zorin, O. Gattering, A. Ebner, M. Brandstetter, *Opt. Express* **2022**, 30, 5222.
- [164] H. Lyu, Z. Wang, Z. Zhang, J. Li, H. Li, Y. Liu, presented at Asia Communications and Photonics Conference (ACP), Shenzhen, China, April **2023**.
- [165] Z. Zheng, X. Ren, K. Zhu, D. Ouyang, J. Wang, C. Guo, G. Du, J. Pei, Q. Lue, S. Ruan, *Opt. Express* **2019**, 27, 37172.
- [166] X. Luo, Y. Tang, F. Dong, J. Wang, L. Yu, P. Yan, J. Wang, Z. Zheng, Q. Lue, C. Guo, S. Ruan, *J. Light. Technol.* **2022**, 40, 4855.

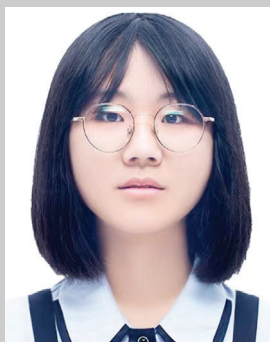
- [167] A. Komarov, H. Leblond, F. Sanchez, *Phys. Rev. A* **2005**, 71, 053809.
- [168] F. Li, P. K. A. Wai, J. N. Kutz, *J. Opt. Soc. Am. B* **2010**, 27, 2068.
- [169] C. R. Giles, E. Desurvire, *J. Light. Technol.* **1991**, 9, 271.
- [170] M. A. Chernysheva, A. A. Krylov, N. R. Arutyunyan, A. S. Pozharov, E. D. Obraztsova, E. M. Dianov, *IEEE J. Sel. Top. Quantum Electron.* **2014**, 20, 448.
- [171] F. X. Kärtner, J. Aus Der Au, U. Keller, *IEEE J. Sel. Top. Quantum Electron.* **1998**, 4, 159.
- [172] T. Wang, W. Ma, Q. Jia, Q. Su, P. Liu, P. Zhang, *IEEE J. Sel. Top. Quantum Electron.* **2018**, 24, 1102011.
- [173] J. Zhou, W. Pan, Y. Feng, *Opt. Express* **2020**, 28, 17424.
- [174] Y. Wang, C. Wang, F. Zhang, J. Guo, C. Ma, W. Huang, Y. Song, Y. Ge, J. Liu, H. Zhang, *Reports Prog. Phys.* **2020**, 83, 116401.
- [175] S. Xu, A. Turnali, M. Y. Sander, *Sci. Rep.* **2022**, 12, 6841.
- [176] J. M. Dudley, L. P. Barry, J. D. Harvey, M. D. Thomson, B. C. Thomsen, P. G. Bollond, R. Leonhardt, *IEEE J. Quantum Electron.* **1999**, 35, 441.
- [177] J. Fellingner, A. S. Mayer, G. Winkler, W. Grosinger, G.-W. Truong, S. Droste, C. Li, C. M. Heyl, I. Hartl, O. H. Heckl, *Opt. Express* **2019**, 27, 28062.
- [178] S. Yang, Q.-Y. Zhang, Z.-W. Zhu, Y.-Y. Qi, P. Yin, Y.-Q. Ge, L. Li, L. Jin, L. Zhang, H. Zhang, *Opt. Laser Technol.* **2022**, 152, 108116.
- [179] W. Liu, L. Pang, H. Han, W. Tian, H. Chen, M. Lei, P. Yan, Z. Wei, *Opt. Express* **2015**, 23, 26023.
- [180] E. M. Dianov, *Light Sci. Appl.* **2012**, 1, e12.
- [181] J. Zou, C. Dong, H. Wang, T. Du, Z. Luo, *Light Sci. Appl.* **2020**, 9, 61.
- [182] M. R. Majewski, R. I. Woodward, S. D. Jackson, *Opt. Lett.* **2019**, 44, 1698.



**Kuen Yao Lau** is currently an associate professor at Soochow University, China. He obtained his Ph.D. in Photonics Engineering in February 2018 at the University of Putra Malaysia. He was a post-doctoral researcher at Universiti Tenaga Nasional, Malaysia (2018–2019), Aalto University, Finland (2019–2020), and Zhejiang University, China (2021–2024). His research interests include fiber lasers, nonlinear, and ultrafast optics. He was awarded with the Wiley China Open Science High Contribution Author in November 2022.



**Zhichao Luo** received his Ph.D. degree from the School of Information and Optoelectronic Science and Engineering, South China Normal University China in 2012. Later, he joined Guangdong Provincial Key Laboratory of Nanophotonic Functional Materials and Devices, School of Information and Optoelectronic Science and Engineering, South China Normal University, China as a lecturer and associate professor. Currently, he is a professor at the School of Information and Optoelectronic Science and Engineering, at South China Normal University, China. His research interests include fiber lasers, nonlinear optics, optical solitons, microfiber devices, and comb filters.



**Jinwen Lin** is studying for her Bachelor's degree at the College of Optical Science and Engineering, Zhejiang University. Currently, she is a research assistant at the College of Optical Science and Engineering, Zhejiang University. Her research interests include optical fiber lasers, artificial saturable absorbers, pulsed lasers, mode-locking, and ultrafast optics.





**Beibei Xu** received his Ph.D. degree from Zhejiang University, China in 2014. He continued his post-doctoral study at Kansas University from 2014 to 2015, then at Temple University from 2015 to 2016, and at Maryland University from 2016 to 2018, USA, focusing on optoelectronic properties of inorganic and organic semiconductor nanomaterials. He joined the University of Washington as a research associate in 2019. Then, he started his career as a PI at the College of Optical Science and Engineering, Zhejiang University in Sep. 2019, where he directed his research on perovskite luminescent materials and devices, the interaction of femtosecond laser with matter.



**Xiaofeng Liu** received his Ph.D. degree in Materials Science from the Shanghai Institute of Optics and Fine Mechanics, Chinese Academy of Science China in 2011. Later, he joined Frontier Research Center, Tokyo Institute of Technology Japan, and Max Planck Institute of Colloids and Interfaces Germany as a Humboldt post-doctoral fellow. Currently, he is an associate professor at the School of Materials Science and Engineering, Zhejiang University, China. His research interests include optical properties of materials and nonlinear optical properties and devices.



**Jianrong Qiu** is currently a chair professor at Zhejiang University, China. He received his Ph.D. in Materials Science from Okayama University, Japan in 1992. He has been honored with an Academic Award from the Ceramic Society of Japan in 2007, the Otto-Schott Research Award from the Ernst Abbe Fund, Germany in 2005, the Kurata Award from the Ceramic Society of Japan in 2002, the Outstanding Young Researcher Award from the Natural Science Foundation of China in 2001, and Adachi Award from the Rare-earth Society of Japan in 1999. He received an Honorary Doctoral Degree from Aalborg University, Denmark in 2016. Qiu is a member of the ACerS Glass and Optical Materials Division and received the G. W. Morey Award in 2015. His research interests are light interaction with materials (Laser 3D printing and fs laser micro-processing), and optoelectronic materials especially glasses and glass ceramics, luminescent and nonlinear optical materials.